JOURNAL OF GEOPHYSICAL RESEARCH, VOL. 104, NO. B5, PAGES 10,667–10,694, MAY 10, 1999

Structure of an island-arc: Wide-angle seismic studies in the eastern Aleutian Islands, Alaska

Moritz M. Fliedner[1] and Simon L. Klemperer

Department of Geophysics, Stanford University, Stanford, California

Abstract. New seismic wide-angle data from the eastern Aleutian Islands show a mafic composition and a 30-km-thick island-arc crust. Traveltimes of P and S refracted arrivals and prominent crustal and mantle reflectors observed to offsets of over 300 km were used to derive velocity models for the eastern Aleutian Arc between the islands of Atka and Unimak using a three-dimensional finite difference modeling and tomography code. We interpret the highest crustal P wave velocities of 7.2–7.4 km/s between about 12 and about 22 km depth to the south and north of the main volcanic line as remainders of preexisting oceanic crust into which arc magma is intruded. Apart from the pieces of oceanic crust, the velocities suggest an overall mafic composition for the arc, composed mainly of metabasalts, diorite and diabase in the upper crust, and garnet-granulite or amphibolite-to-hornblendite in the lower crust. Reflected arrivals from the subducting Pacific plate at depths of 45–55 km beneath the fore-arc, together with P_n, show a mantle wedge with P wave velocities as low as 7.4 km/s, increasing with depth to about 8.1 km/s with an average of about 7.7 km/s. A mantle composition that grades from mainly pyroxenite (probably ultramafic cumulates) near the Moho to dunite at greater depths best explains these observed velocities.

1. Introduction

Phanerozoic continental crust is widely believed to grow mainly by the accretion of magmatic arcs [e.g., *Hamilton,* 1981], although direct accretion of oceanic crust (ophiolites), basaltic underplating of the crust, and plume-related intraplate magmatism certainly play a role [*Taylor and McLennan,* 1995]. The arc-accretion model, at least in its simplest form whereby complete arcs are added in continental collisions, works only if the composition of magmatic arcs is the same as that of average (Phanerozoic) continental crust. A comparison of mean crustal velocities of island arcs and the continents [*Smithson et al.,* 1981] argues strongly against the simple accretion model; their mean P wave velocity of 6.3 km/s in the continents corresponds to a mean composition of granodiorite, whereas their mean velocities of 6.5–6.9 km/s in island arcs correspond to andesitic composition.

The main uncertainty in existing estimates of average crustal composition is what range of compositions exist in the lower crust. For example, the relative abundance of mafic versus ultramafic rocks in magmatic arcs and continents is poorly known. It is therefore unclear whether other processes such as magmatic underplating or delamination of the lower crust are necessary in order to explain the full crustal structure and composition of continental crust (for a more detailed discussion, see, e.g., *Kay and Kay* [1993], *Nelson* [1991], *Reymer and Schubert* [1984], or *Holbrook et al.* [1992]). The best test to determine the composition of in situ crust is its detailed seismic velocity structure, but, although many velocity measurements have been made of continental crust worldwide, few modern controlled-source data sets exist for oceanic island arcs because their remoteness poses logistical difficulties (one recent seismic study did investigate the purely oceanic Izu-Ogasawara arc system [*Suyehiro et al.,* 1996]). Thus no clear geophysical test of the equivalence of island-arc crust and average continental crust has yet been made.

In July 1994, a large-scale, active-source deep seismic experiment to study the generation of continental crust in island arcs was conducted in the region of the Aleutian volcanic arc and the back-arc Bering Shelf. We measured the seismic-velocity structure of a petrologically well-studied island-arc system in order to provide constraints on continental growth and composition.

This paper focuses on the deep structure of the oceanic eastern Aleutian Arc (the Aleutian Ridge) up to the ocean-continent transition near Unimak Island (Figure 1). Specifically, the wide-angle data recorded along

[1]Now at Bullard Laboratories, University of Cambridge, Cambridge, United Kingdom.

Paper number 98JB01499.
0148-0227/99/98JB-01499$09.00

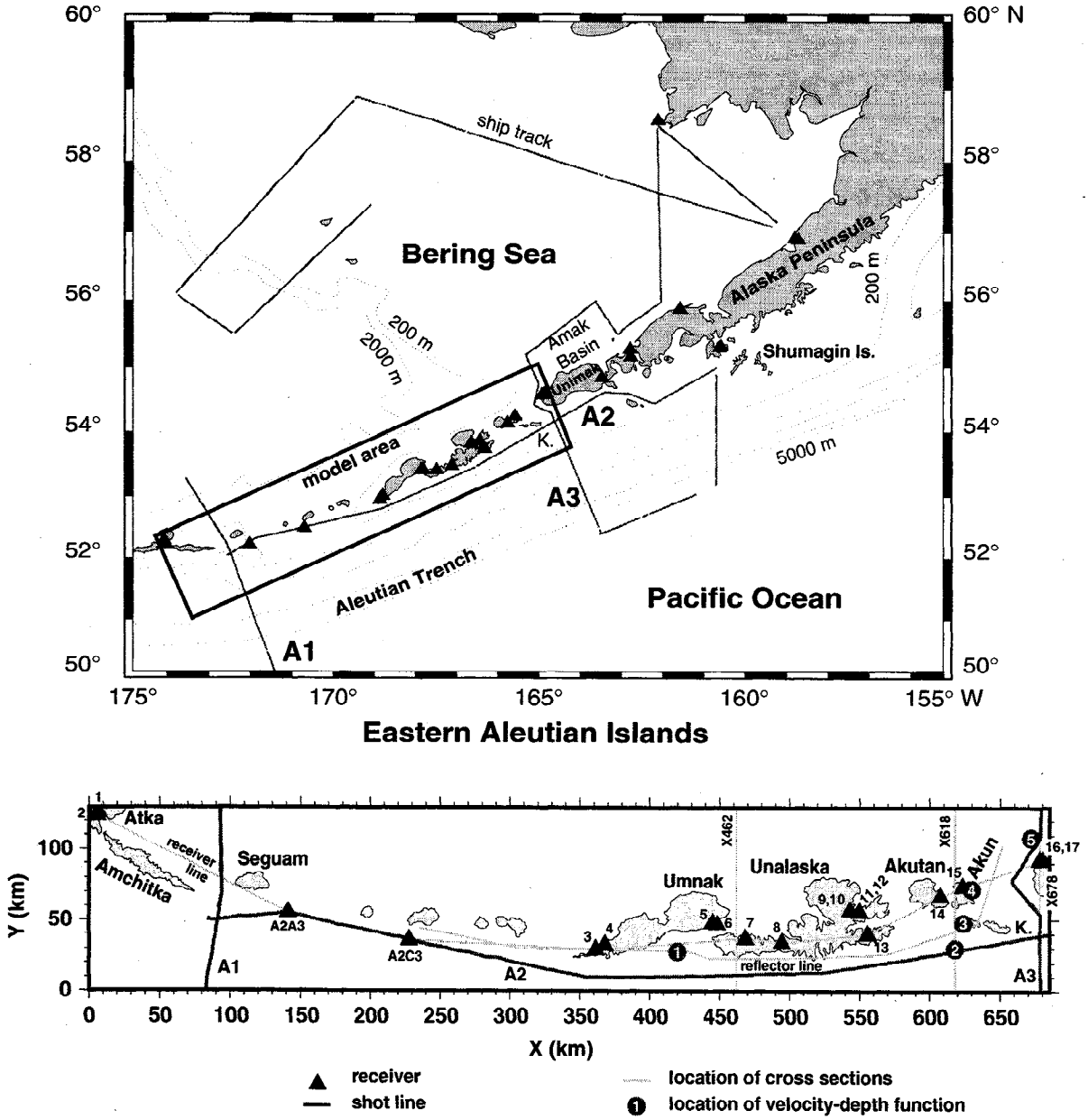

Figure 1. Map of the study area in southwestern Alaska. Land recording stations and two OBS locations used in this study are shown as black triangles (numbered as in Table 1). Bathymetry is indicated by dotted lines. Detail map shows the area of three-dimensional velocity model and locations of cross sections and velocity-depth functions in this paper. K. are the Krenitzin Islands.

the strike of the arc by primarily the on-land PASSCAL array will be used in this analysis.

2. Previous Work in the Aleutians

The continental crust on which the easternmost Aleutian Arc is built is itself mainly an epicontinental Mesozoic island arc platform (Peninsular terrane) and partly accreted continental slope and rise (Chugach terrane) [*Vallier et al.*, 1994]. The oceanic crust on which the arc to the west of Unimak Island is built is a piece of captured about 110-Ma-old Kula plate (Aleutia microplate) [*Marlow and Cooper*, 1983] that forms the floor of the western Bering Sea [*Cooper et al.*, 1976]. Pacific Ocean crust of Paleocene age is currently being subducted beneath the eastern Aleutians at a rate of 75–90 mm/year in a direction nearly normal to the arc [*Creager and Boyd*, 1991; *Vallier et al.*, 1994]. The Wadati-Benioff zone dips about 60° in the central Aleutians and the slab reaches a depth of about 80 km beneath the active volcanos [*Engdahl and Gubbins*, 1987; *Boyd and Creager*, 1991]. Arc magmatism in the Aleutians started probably in early to middle Eocene (55–50 Ma) [*Scholl et al.*, 1987]. The width of the Aleutian Ridge is

about 100 km at Unalaska Island. The ridge seems to have formed in three major phases, recorded in three chronostratigraphic rock series: the lower (55?–37 Ma), the middle (37–5.3 Ma), and the upper (< 5.3 Ma) series. Whereas the Eocene lower series forms the base of the ridge over its entire width, magmatism has been greatly reduced and restricted to the ridge crest since the Oligocene [*Scholl et al.*, 1987].

The most widely used geophysical model of the Aleutian Arc to date is that by *Grow* [1973], which is partly based on data and models by *Shor* [1964] and *Carder et al.* [1967]. It consists of a 7-km-thick upper crust with P wave velocities below 6.6 km/s and a lower crust with velocities of 6.6–6.9 km/s at the top. The Moho is at 25 km depth under the volcanos and the sub-arc mantle velocity is 7.8 km/s. Higher crustal velocities in the fore-arc (about 7 km/s) were found by *Abers* [1994], and coincide with the fore-arc free-air gravity high that is typical of arc systems world-wide.

3. The Seismic Wide-Angle Data set

The experiment's three components included multichannel reflection acquisition, OBS/OBH (ocean-bottom seismometer and hydrophone) deployments, and PASSCAL portable seismograph deployments on land. The *R/V Ewing's* 8400 cubic inch airgun array provided the source. The experiment was a collaborative effort between the University of Delaware, Lamont-Doherty Earth Observatory, University of Texas at Austin Institute for Geophysics, Woods Hole Oceanographic Institution, and Stanford University.

In the wide-angle refraction and reflection part of the experiment 27 portable 3-component Reftek seismometers with 4.5-Hz geophones were deployed on the islands Atka, Umnak, Unalaska, Akutan, Akun, and Unimak, on the Alaska Peninsula between Cold Bay and Port Heiden, at Sand Point in the Shumagin Islands, and at Cape Newenham north of Bristol Bay (Figure 1; Table 1). These seismometers recorded the airgun shots of the reflection survey up to distances of 450 km (300 km in the island arc section). Typically, two seismometers were located closely adjacent to aircraft landing areas in the eastern Aleutians to provide redundancy against equipment failure. Refracted P and S wave arrivals provide seismic velocity information from the crust and uppermost mantle. Reflections from the arc and the subducting Pacific plate (P_sP) give additional insight into the large-scale tectonic structure of the region.

The marine multichannel reflection survey that provided the seismic sources for our wide-angle recordings is described by *McGeary et al.* [1995]. The following ship tracks will be mentioned in this paper (Figure 1): the island arc cross-line A1, the continental arc cross-line A3 and the strike-line A2. Most of the data are from line A2; the following analysis thus primarily discusses this along-arc profile.

Line A2 extends along Pacific (fore-arc) side of the arc

Table 1. Locations of the 27 Land Seismometer Stations

	Name	Latitude	Longitude	Elevation, m
1	Atka 1	52.2309	-174.2223	50
2	Atka 2	52.2040	-174.2080	100
3	Nikolski 1	52.9243	-168.9197	50
4	Nikolski 2	52.9735	-168.8518	150
5	Fort Glenn 1	53.3947	-167.9060	50
6	Fort Glenn 2	53.3949	-167.8479	10
7	Chernofski	53.3889	-167.5146	50
8	Kashega	53.4585	-167.1387	25
9	Captains Bay 1 (Unalaska)	53.8254	-166.6055	45
10	Captains Bay 2 (Unalaska)	53.8260	-166.6048	30
11	Iliuliuk 1 (Unalaska)	53.8417	-166.5062	95
12	Iliuliuk 2 (Unalaska)	53.8409	-166.5070	100
13	Beaver Inlet	53.7296	-166.3266	30
14	Akutan	54.1359	-165.7644	25
15	Akun	54.2476	-165.5770	50
16	Cape Sarichef 1	54.5877	-164.9061	85
17	Cape Sarichef 2	54.5920	-164.8766	210
18	False Pass	54.8508	-163.4301	5
19	Izembek (Cold Bay)	55.2970	-162.7903	5
20	Mount Simeon (Cold Bay)	55.1856	-162.7860	120
21	Sand Point 1	55.3238	-160.5031	60
22	Sand Point 2	55.3179	-160.5151	30
23	David River 1	55.9094	-161.6368	20
24	David River 2	55.9117	-161.6369	15
25	Port Heiden 1	56.9443	-158.5743	35
26	Port Heiden 2	56.9671	-158.6677	15
27	Cape Newenham	58.6438	-162.0502	200

from Seguam Pass to the Shumagin Islands. Although it runs mostly above the arc platform in very shallow water well arcward of the accretionary wedge and fore-arc basins, we will call this area simply "fore-arc" in the following discussion. The line is well recorded on all stations on the oceanic Aleutian Ridge (stations 1 to 15, Atka to Akun) but not on the other stations. This introduces a coverage bias towards the fore-arc for the oceanic island arc compared to the continental Peninsula section.

Line A3 crosses the arc via Unimak Pass where the continental margin of the Bering shelf intersects the Aleutian Ridge. Unimak Pass therefore marks the transition to the continental arc. Line A3 extends from the Pacific plate northward across the Aleutian Trench, and across the arc between the islands Akun and Unimak into Amak basin, the southernmost of the Bering shelf marginal basins. This line was recorded by the two in-line stations at Cape Sarichef (receivers 16 and 17), by all stations (1–15) to the west, and by the three closest stations to the east (at False Pass and Cold Bay, receivers 18–20; these stations are outside the area considered in this paper—see locations in Table 1). Shots from this line were also recorded in a 2-D OBS/OBH line and analyzed by *Lizarralde et al.* [1996].

Line A1, although recorded on the five westernmost land stations, yielded data of usable quality only on receivers 1 and 2 on Atka. Our database for a cross section perpendicular to the strike of the the purely oceanic island arc is thus essentially a single fan recording with a minimum offset of about 70 km and therefore of limited use for interpretation of the crust. This transect is analyzed in detail by *Holbrook et al.* [1994] based on OBS/OBH recordings.

Examples of the data quality of the on-land data and typical phases seen in the receiver gathers are displayed in Figures 2 and 3. Figure 2a shows the variable character of P_n, which is a clear phase looking eastward, but is practically absent looking westward where the first recognizable phase is the P_mP reflection; modeled traveltimes for arrivals from the east are shown on a detailed view (Figure 3a) from the neighboring receiver. Figure 2b shows several clear secondary phases, P wave reflections as well as S waves. The reflected phases are shown in more detail together with an overlay of the modeled arrival times in Figures 3b and 3c. The P_mP and at least one later reflection from the mantle ($P_{mr}P$; see Figure 4 for terminology) form bright distinct arrivals looking east (Figure 3c) compared with a fuzzier appearance looking west (Figure 3b), although it is easier to separate two mantle reflections, the later one being the slab reflection P_sP, on the western branch of the record. On both branches, the first arrival becomes weak beyond about 100 km offset (it would be expected to be approximately horizontal at just under 3 s on the reduced traveltime plot; P_4 in Figure 3c).

Figure 2c provides a direct comparison of strike (A2) and dip line (A3) recordings, showing that some events like the crustal reflection P_5P can be easily correlated between the two lines. Two remarkable features of the dip line recording are also shown in detail in Figure 3d: the large delays of the first arrival (P_3, P_4) due to the back-arc sedimentary basin north of the active volcanos (the location of the receiver is in the volcanic line on the east slope of Akun volcano), and the disruption of all later arrivals by a strong diffraction tail apparently originating from the termination of P_5P in the volcanic line. The strongest and most continuous example of S wave arrivals is displayed together with an overlay of the modeled P and S arrival times on the record in Figure 3e; receiver 13 recorded line A2 from essentially the same along-strike position as receiver 9 (Figures 2b, 3b, and 3c) but 20 km closer to the ship track.

4. Recording and Processing

The land receivers were three-component 4.5-Hz geophones connected to Reftek digital seismographs in continuous recording mode. The instruments recorded for up to 2 weeks at a rate of 100 samples/s. The sensors were either buried about 75 cm in firm soil, or plastered to bedrock or building foundations, and oriented with respect to magnetic north. The exact location of each station was determined by averaging the horizontal positions provided by the internal GPS (Global Positioning System) clock every hour. The rms-error of the GPS position time series was about 30 m for a 1-week recording period. Station elevation was measured from USGS topographic maps at scales of 1:63,360 or 1:250,000. The continuous data were cut into receiver gathers according to the shot timing of the MCS survey. These gathers are available from the IRIS Data Management Center (http://www.iris.washington.edu/).

The displayed data are band-pass filtered 2–10 Hz. For the picking of later arrivals, we also applied a minimum-phase predictive deconvolution. The displayed gathers have a trace-length AGC applied in order to equalize the mean amplitudes across the gather.

5. Data Analysis, Compressional Wave Arrivals

We used traveltimes of refracted and reflected arrivals from all stations to derive a velocity model for the crust, and where possible, upper mantle. The crustal arrivals can in general be broken up into four refracted phases P_1–P_4 and their associated reflections P_1P–P_4P (Figure 4). P_1 and P_2 (sedimentary and volcanic cover with velocities between 2 km/s and 5 km/s) are observed as first arrivals only at the short offsets provided by the OBSs (Figure 5), but occasionally show up on land stations as strong secondary arrivals (multiple reflections and refractions within the top layers); the crossover distance for P_3 is 30–40 km. P_3 with a velocity of about 6 km/s represents the upper (igneous) crust and P_4 with velocities around 7 km/s the midcrust to lower

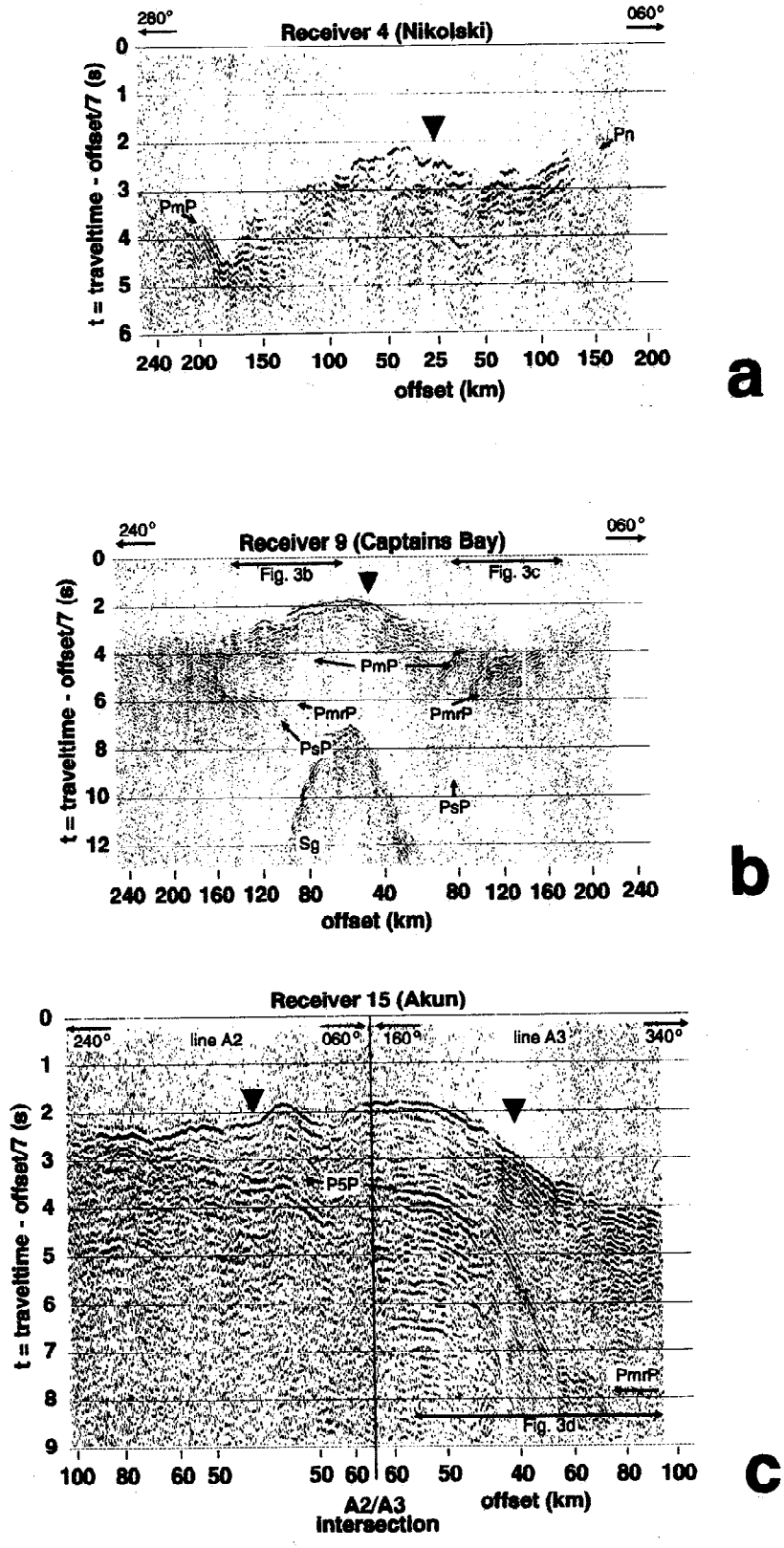

Figure 2. Four example receiver gathers of the 27 recorded. Every fifth trace of the vertical (except Figure 2d) component is plotted with constant trace spacing (nonlinear offset scale) against reduced traveltime (reduction velocity is 7 km/s for vertical component, 4 km/s for horizontal components. Solid triangles mark closest point of approach of source ship to receiver. (d) Overlay on transverse component shows the modeled traveltime of the refracted S wave and predicted S wave two-way traveltime to P wave reflectors 5 and m (Moho). Phases labeled as defined in Figure 4.

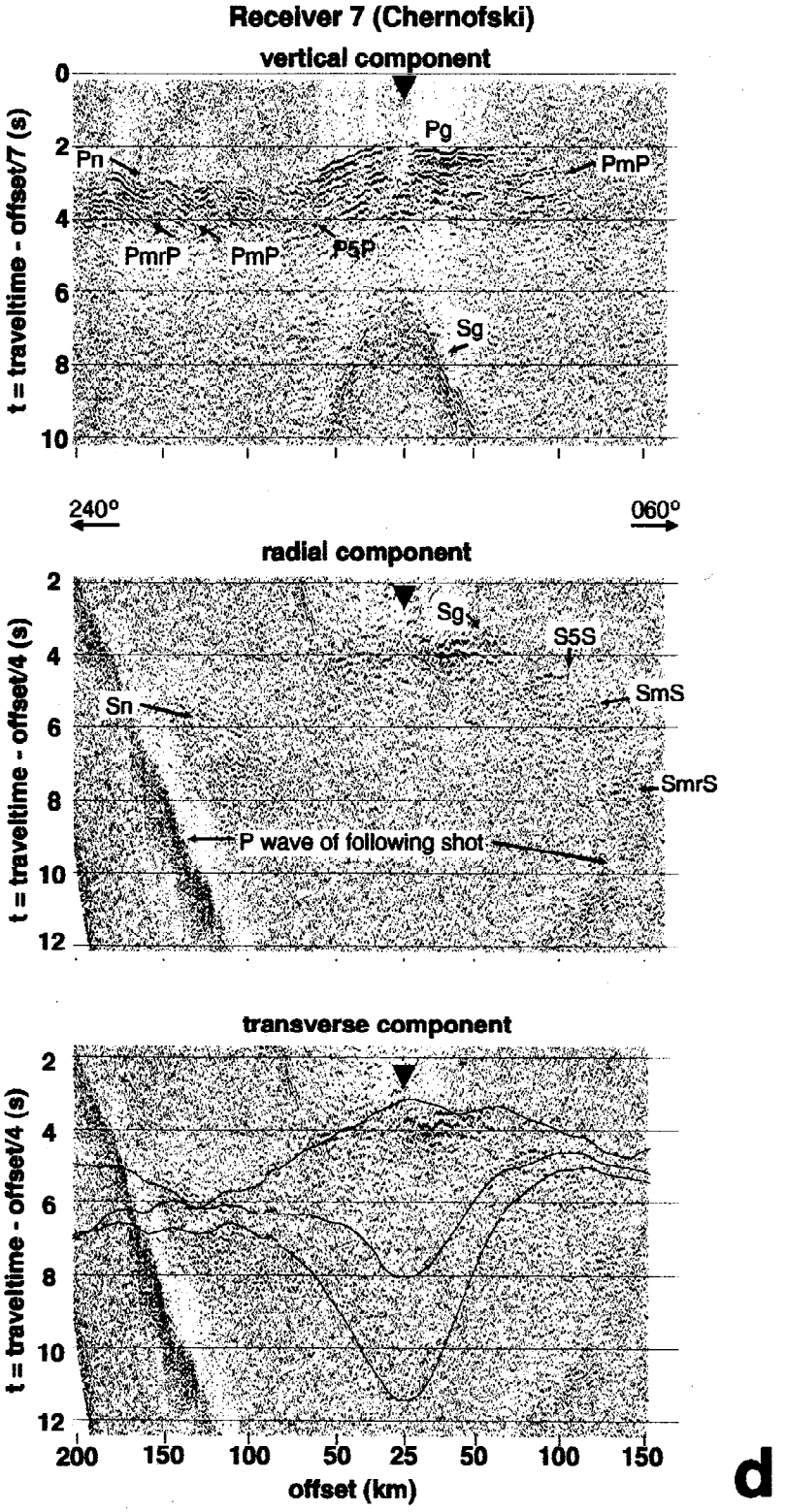

Figure 2. (continued)

crust. The boundary between upper and middle/lower crust usually generates a wide-angle reflection at near-critical offsets (P_4P). The peak amplitude of P_3 usually drops drastically between the critical distance and the crossover distance of P_4. The clearest P_n is observable at Nikolski (receivers 3 and 4; Figures 2a and 3a) with a crossover distance of 132 km.

With the exception of the Cape Sarichef stations (16 and 17) in line A3 and the two OBSs in line A2, all our stations recorded in a broadside fan geometry. We therefore used a three-dimensional finite difference code to model traveltimes and invert for velocity [*Vidale*, 1990; *Hole*, 1992; *Hole and Zelt*, 1995]. This procedure allows us to do tomography on a densely sam-

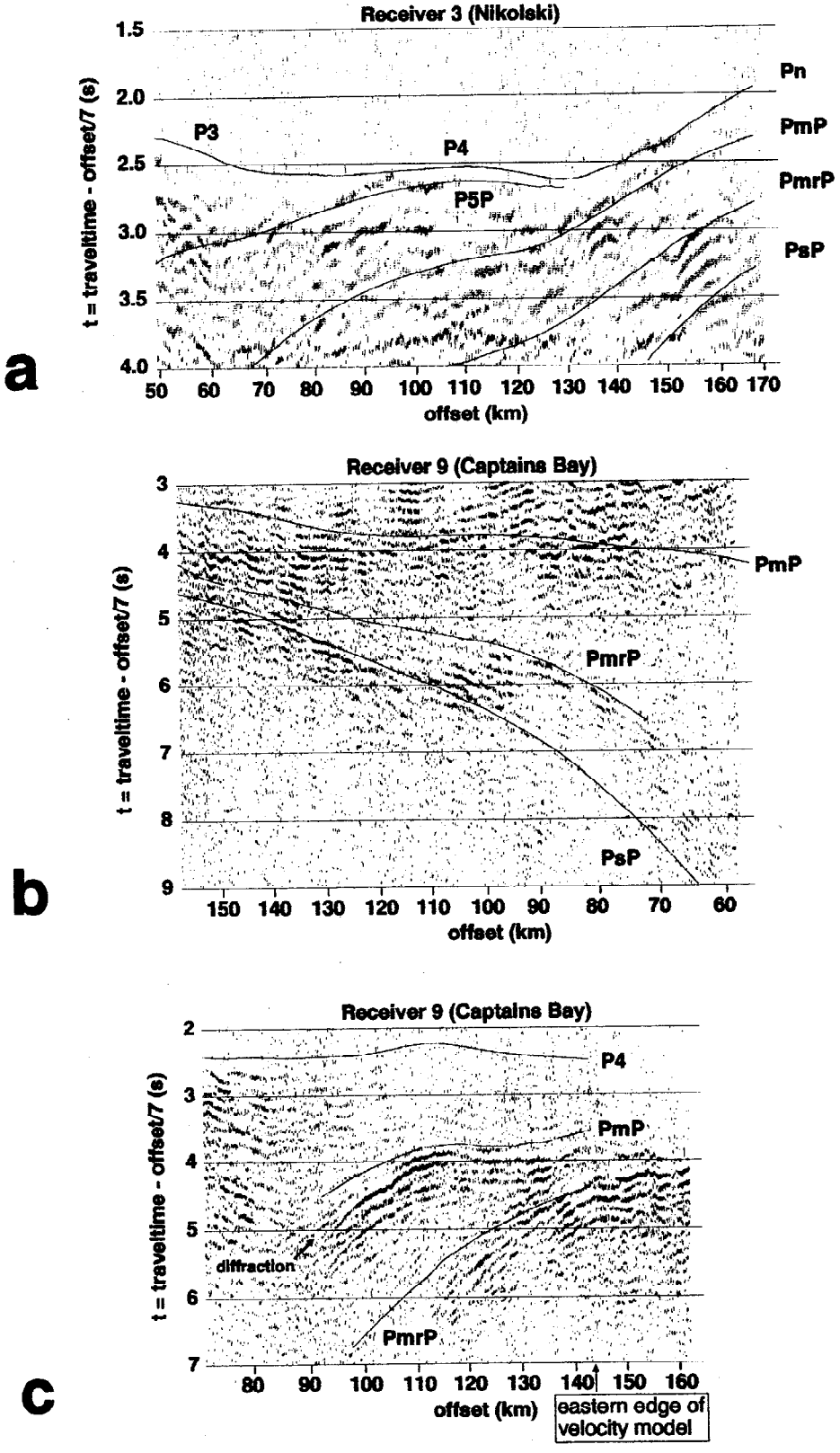

Figure 3. Details from different receiver gathers. Vertical component traces plotted with constant trace spacing (nonlinear offset scale) against reduced traveltime (reduction velocity is 7.0 km/s). Triangles mark projection of receiver locations on shot line. Modeled traveltimes shown as solid lines. (a) receiver 3 (Nikolski) recording line A2 from the east; (b) receiver 9 (Captains Bay) recording line A2 from the west; (c) receiver 9 recording line A2 from the east; (d) receiver 15 (Akun) recording line A3; (e) receiver 13 (Beaver Inlet) recording line A2. Phases labeled as defined in Figure 4.

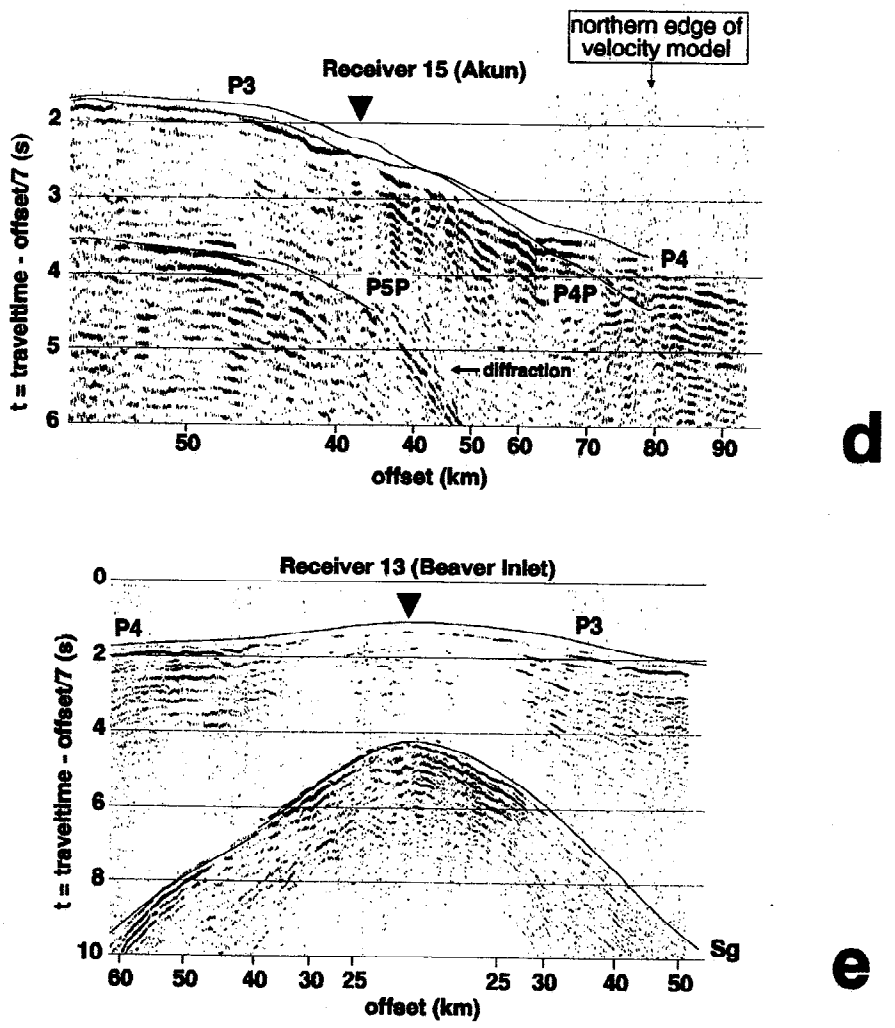

Figure 3. (continued)

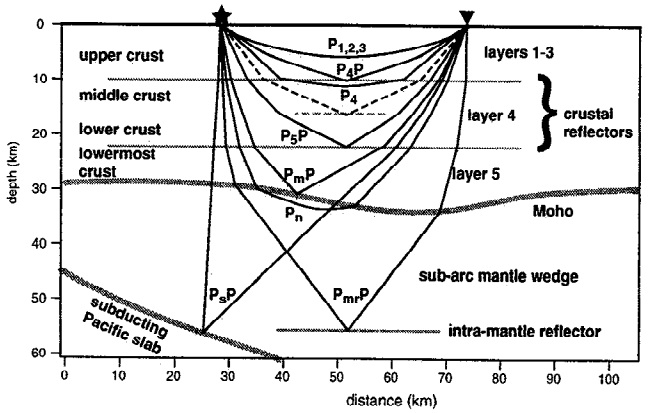

Figure 4. Schematic drawing of ray paths used in this study between an offshore shot (star) from line A2 into a receiver (triangle) on land. The three uppermost layers of the crust are only seen at short offsets on the OBSs and therefore not shown separately here. P_x are refracted arrivals through layer x (P_n is traditionally used for the upper-mantle phase), P_xP are wide-angle reflections from reflecting surface x. The lowermost crustal layer 5 produces a wide-angle reflection, but not a refraction that becomes a first arrival between P_4 and P_n. Dashed lines indicate unnamed crustal reflectors that are not tied to a specific refracted phase or velocity increase.

pled velocity model (node-spacing 1.2 km) with both refracted and reflected arrivals. The velocity model is oriented so that the X axis coincides with the general strike direction of the arc. The tomographic inversion is a nonlinear iterative ray-tracing scheme in which, after each update of the model, the ray path is determined anew in the forward modeling step. During the inversion, the perturbations added to the velocity field are spatially smoothed with filters of decreasing size. The final filter half-width size was 12 by 6 by 1.2 km, so any anomalies smaller than this cannot be resolved (see e.g., Figure 5 at 50 km and 2.8 s—this anomaly is represented also by the bright red and blue stripes at shotpoint 13,100 for A2A3 in Plate 2; or Figure 15 at 40 km and 5.3 s). We used refracted (first) arrivals to invert for velocity only, and reflected arrivals to invert both for velocity (P_mP and P_sP) and depth to the reflecting interface: P_4P, P_5P (a lower-crustal reflector beneath the turning depth of crustal refracted arrivals), P_mP, $P_{mr}P$ (a bright mantle reflector), and P_sP (the reflection from the subducting Pacific plate; Figure 4) using the method of *Hole and Zelt* [1995]. The reflector-depth inversion is based on the assumption that reflections from greater depth arrive at a later time. This

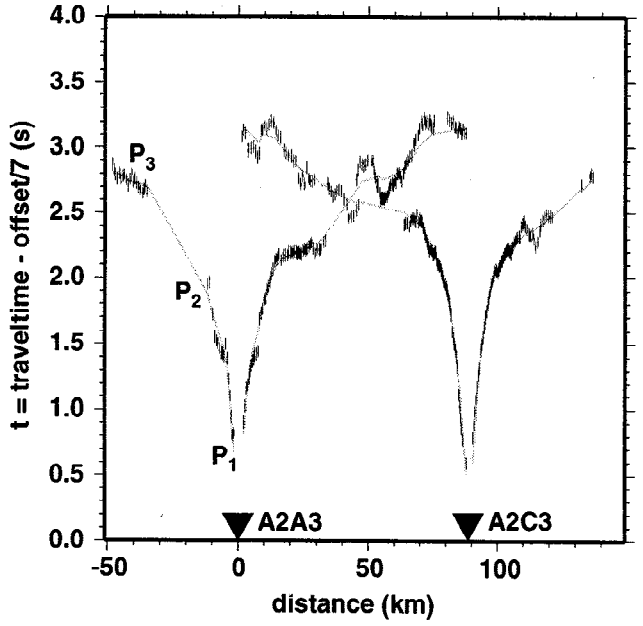

Figure 5. Picked (black bars) and modeled (solid lines) traveltimes of the OBS first arrivals reduced at 7.0 km/s. Only every tenth pick is plotted. Distances are offsets relative to OBS A2A3.

assumption breaks down at large offsets where deep reflections arrive earlier than shallow ones due to the increase of velocity with depth. Near the crossover point of a shallow and deep reflection, the traveltimes alone are obviously useless for depth determination, and beyond the crossover the reflector geometry can only be determined by trial-and-error modeling.

Shallow arrivals were used first to determine the shallow layers of the model. While inverting the deeper arrivals, we kept the previously determined parts of the model fixed ("layer-stripping"). The ray coverage of picked P and S arrivals is shown in Plate 1 by summing the ray hit count in each cell of the P and S wave models along the axis perpendicular to the projection plane. Traveltime misfits for the modeled first arrivals are summarized in Plate 2. The overall rms-error for the first arrivals is 73 ms (compared to an overall picking error of about 100 ms), for the S arrivals 70 ms, for the Moho reflection P_mP 104 ms, and for P_sP 177 ms.

The first arrivals from the upper crust (P_3) penetrate to a depth of about 8 km although we cannot resolve the shallow structures (except for a delay time or average velocity) due to the lack of short offset information away from the two OBS stations (Figure 5). A shallow (depth penetration < 150 m) seismic refraction survey on Akutan (Figure 1) [*Motyka and Nye*, 1988] found 4.2 and 4.9 km/s for the volcanic bedrock close to the surface. This is presumably a reasonable estimate of the surface velocity at all stations in the arc.

The penetration depth of P_3 provides an estimate for the minimum thickness of the upper crust of 8–10 km. This is corroborated by the results of P_4P reflector modeling, which yields depths to the upper crustal reflector of 8–16 km. P_4P is the shallowest reflector that can be traced near the critical points on the land gathers, but the offsets are too wide to provide more than an approximate depth in most places.

Crustal rays turn mainly in three different depth ranges: about 7 km (6.3 km/s), about 10 km (6.5–6.7 km/s), and about 15 km (6.9–7.0 km/s). P_4 penetrates to a maximum depth of 25 km west of Umnak, which is therefore the minimum thickness of the arc crust (Plate 1; X $\approx$ 350 km).

Since the land receivers mainly recorded long offsets, reflected arrivals from the lower crust and upper mantle are predominant in the gathers. The receivers and the observed midpoints for shots from line A2 cover a surface area that lies between 50 and 100 km above the subducting slab. The land stations are situated 60–80 km above the Wadati-Benioff zone of hypocenters [*Espinosa and Rukstales*, 1988] (see also Figure 6). Because of the dip of the slab, the recorded P_sP reflections bounce from a much shallower part of the slab near the ship track (Figure 6). Nevertheless, it is remarkable to trace this reflection 150 km (reflection-point location) north of the trench to a depth of about 55 km. *Brocher et al.* [1994] traced the megathrust 200 km from the trench on the TACT line in the Gulf of Alaska but only to a depth of about 30 km; *Fisher et al.* [1983] possibly imaged the very shallow (12 km) Pacific slab 275 km arcward between Kodiak Island and the Kenai Peninsula with near-vertical data. *McGeary et al.* [1995] traced the slab reflection nearly continuously along the 800 km of profile A2; our P_sP arrival is the wide-angle recording of the same event.

Wide-angle reflectivity is strongest at arrival times that fall between the expected Moho P_mP arrival and the arrival of the slab reflection P_sP. This reflectivity is often quite diffuse especially in the central part of the study area (around Umnak Island). At least one distinctive coherent reflection ($P_{mr}P$) between P_mP and P_sP can be correlated between most stations; it is clearly a mantle arrival (the traveltime does not fit a PS converted arrival) at about 50 km depth (Figures 2b, 2c, 3a, 3b, and 3c). P_mP itself is usually rather weak with the exception of receiver 9 recording shots from the east where a diffraction from a unresolved Moho discontinuity or reflections from thin layers just below the Moho probably enhance the amplitude of the wave train (Figures 2b and 3c).

In Plates 3–7, we present different cross sections through the P and S velocity models. The three across-arc sections were taken at locations with good ray coverage; the two strike lines were taken along the line of receivers (best shallow coverage) and along the lines of reflection points of P_mP between the sources (ship-track) and the receivers (best deep coverage). The shaded and contoured areas are those parts of the model that have been hit by a ray within a radius of 10 grid cells (12 km) in X direction, 5 grid cells (6 km) in Y direction, and 1 grid cell (1.2 km) in depth, which is the size of the final smoothing filter applied to the slowness pertur-

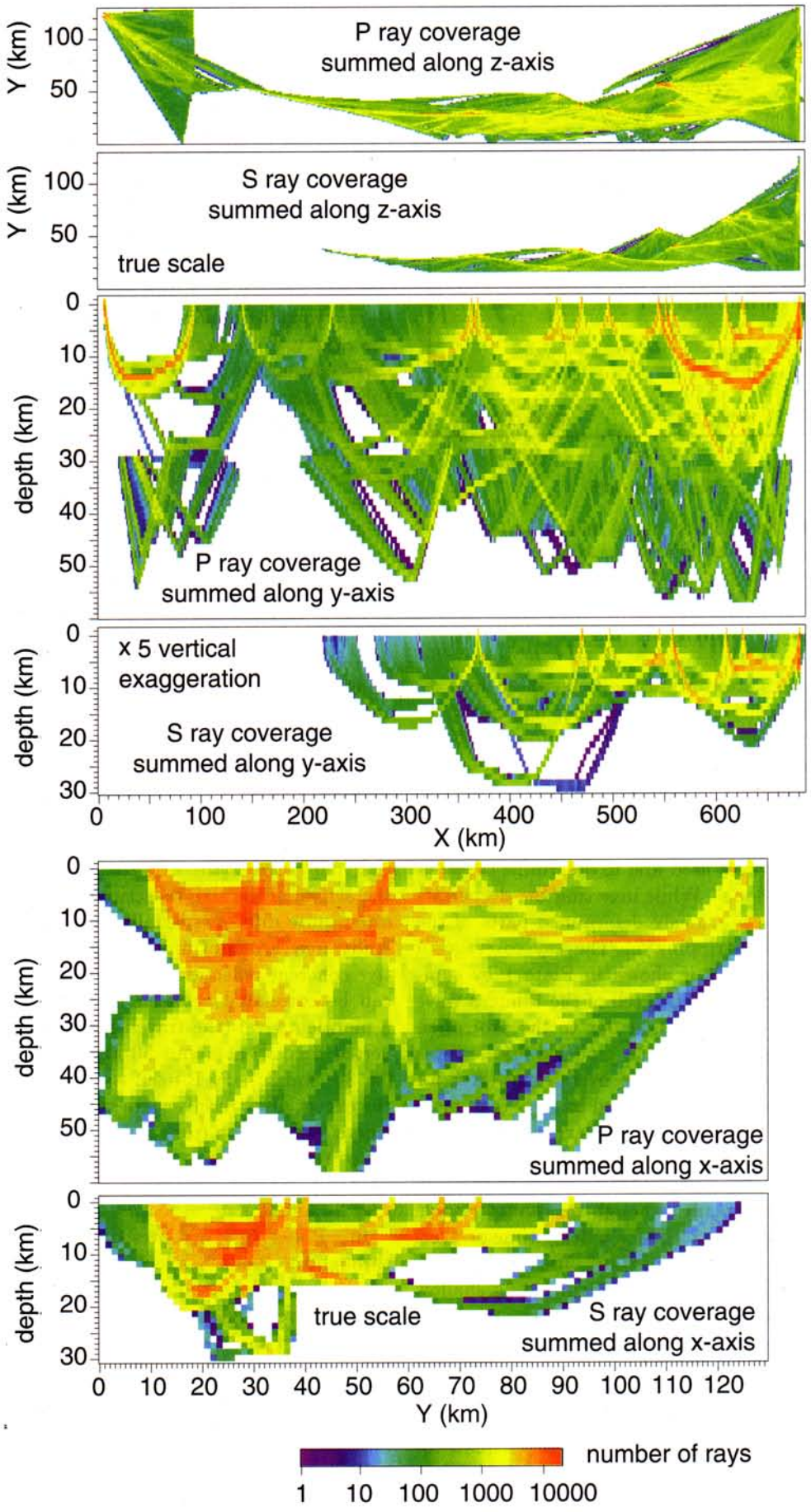
P ray coverage
summed along z-axis
S ray coverage
summed along z-axis
true scale
P ray coverage
summed along y-axis
x 5 vertical
exaggeration
S ray coverage
summed along y-axis
P ray coverage
summed along x-axis
true scale
S ray coverage
summed along x-axis
Y (km)
depth (km)
X (km)
number of rays
1 10 100 1000 10000

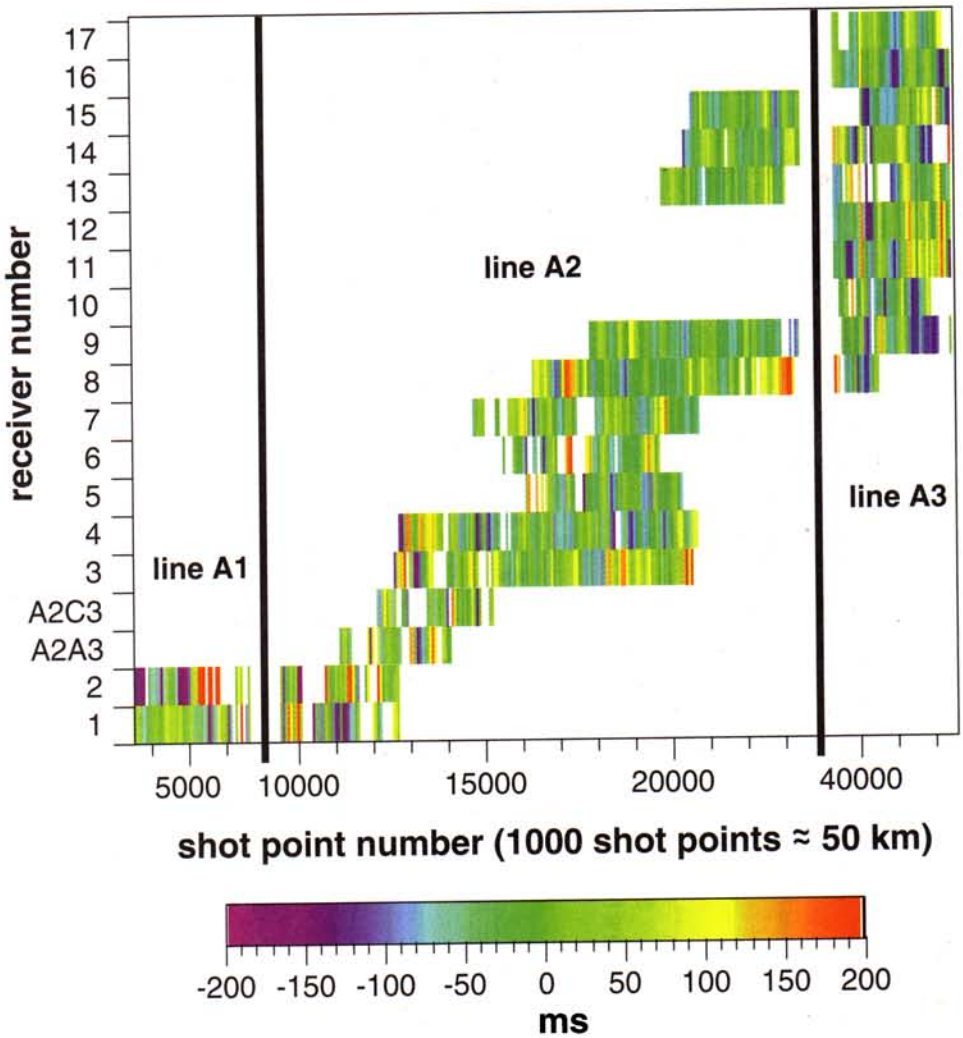

Plate 2. Traveltime residuals of first arrivals (picked first-arrival time minus the first-arrival time calculated with the three-dimensional P wave velocity model in milliseconds) for each receiver, averaged across 10-shotpoint wide bins. Shot point interval is approximately 50 m.

bations in the last inversion steps. Superimposed are the modeled reflectors, the Moho and subducting slab in their entirety (constrained where intersecting with the shaded area), the others only where they are constrained by nearby reflection points. Since the reflectors are modeled as "floating" interfaces, i.e., not tied to a particular velocity discontinuity, they do not always plot exactly on the steepest velocity gradients that presumably gave rise to the reflections.

The modeled crustal reflectors conveniently divide the crust into three parts: an upper crust from 0 to 12 km, which has both good P and S wave coverage, a middle crust from 12 to 22 km, which has fairly good P and some S wave coverage, and a lower crust from 22 to 30 km, which has P reflection coverage but only sparse P refraction coverage and hardly any S wave coverage.

We ran a resolution test (Plate 8) on two checkerboard disturbances to the velocity model by inverting synthetic traveltimes calculated for the same set of source-receiver pairs as in the real inversion. A sinusoidal perturbation of ± 0.2 km/s has been added to a simplified version of our final three-dimensional P wave velocity model; traveltimes have been calculated for this new velocity model; these synthetic traveltimes have been used as input data instead of the real picks for an inversion starting with the unperturbed veloc-

Plate 1. P and S ray coverage for traveltime tomography. In each display, the number of rays is summed along the axis perpendicular to the page and plotted with a logarithmic color code. Refracted ray paths are plotted completely, reflected ray paths only where they were used in the tomography: P_mP between mid-crustal reflector 4 (Figure 4) and the Moho, P_sP between the Moho and the subducting slab.

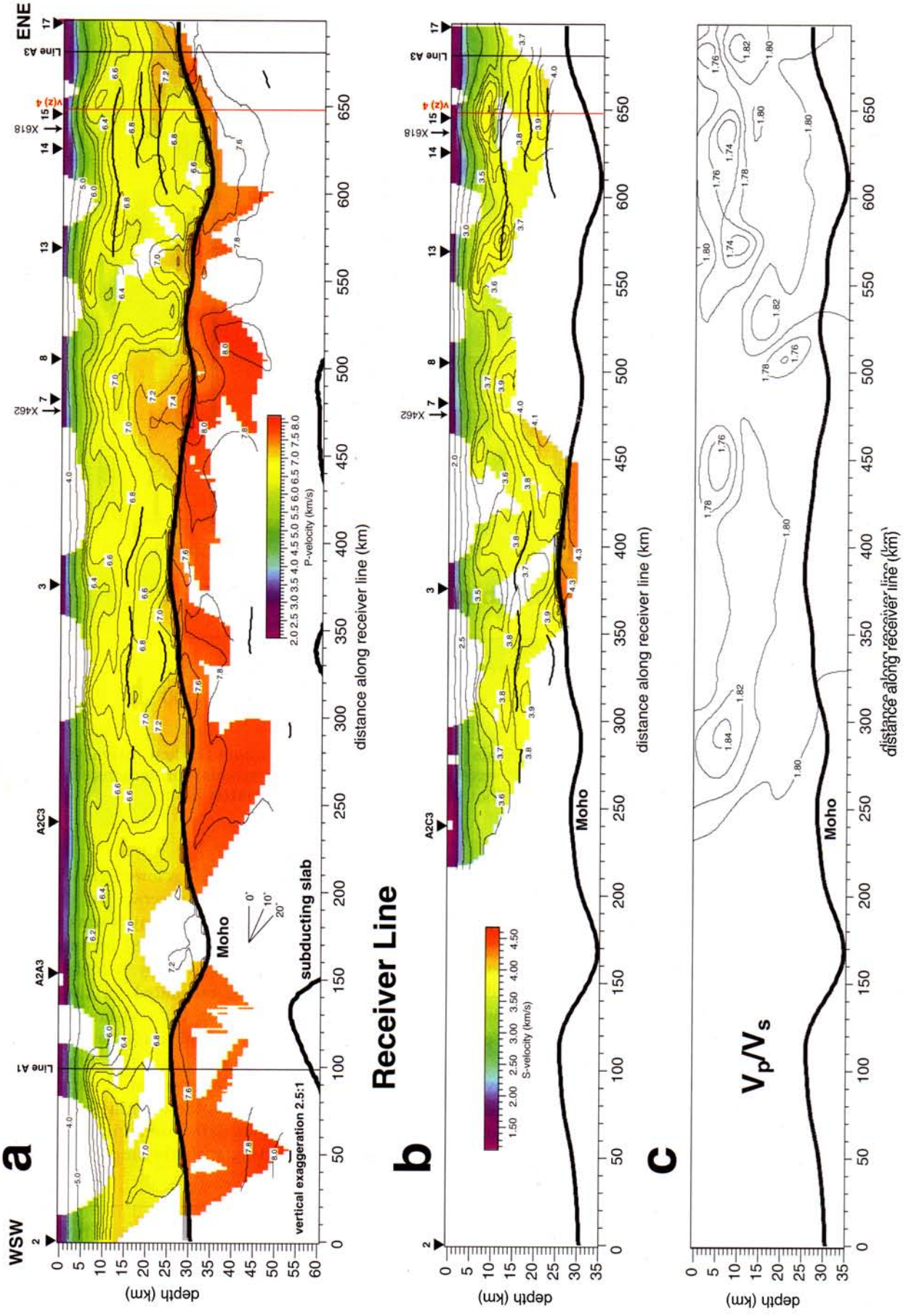
a
WSW
ENE
Line A1
Line A3
A2A3
A2C3
X462
X618
V(z) 4
Moho
subducting slab
vertical exagerration 2.5:1
0°
10°
20°
P-velocity (km/s)
2.0 2.5 3.0 3.5 4.0 4.5 5.0 5.5 6.0 6.5 7.0 7.5 8.0
distance along receiver line (km)
depth (km)
Receiver Line
b
S-velocity (km/s)
1.50 2.00 2.50 3.00 3.50 4.00 4.50
c
V_P/V_S

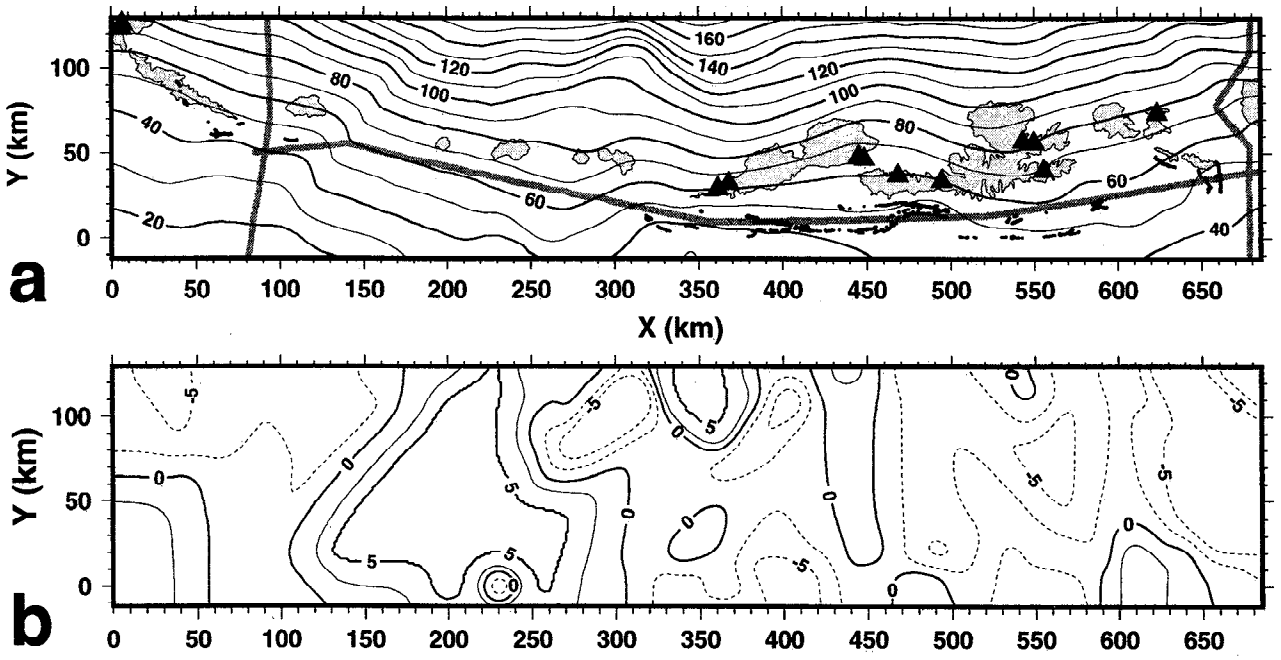

Figure 6. (a) Final depth-contour map of top of subducting Pacific plate. Starting model for the reflector modeling of P_sP traveltimes was the Benioff zone geometry derived by *Espinosa and Rukstales* [1988] (unchanged outside the area of reflection point coverage). Black triangles mark receiver sites where slab arrival was picked, solid gray line is the ship track (shot line), black dots mark locations of modeled reflection points. Contour interval is 10 km. (b) Deviation of final model Figure 6a from starting model in kilometers. Negative contours (final model shallower than starting model) dashed. Contour interval is 2.5 km. Large deviations away from the reflection points are extrapolation artifacts of the gridding procedure.

ity model. The result shows to what degree features in the inverted velocity field can be taken to reflect real structure. While the long-wavelength disturbances are restored quite well where the ray coverage is adequate (e.g., boxes 1 and 2 in Plate 8a), the short-wavelength disturbances are seriously blurred (e.g., boxes 1 and 2 in Plate 8b); the true resolution of the model is therefore somewhere in between the two test cases. Particularly in the mantle where the only constraints are diving waves below the Moho and reflections form the slab, only a bulk velocity estimate can be recovered. For estimates of crustal composition, however, the recovery of a reliable one-dimensional velocity model is more important than resolution of structural details (note e.g., the excellent fit of the modeled P and S refractions in Figure 3e). In the crust where ray coverage is more uniform, the general pattern of velocity highs and lows is recovered in the areas of high ray density (e.g., Plates 8a and 8b between 200 and 400 km at shallow depths; boxes 1 and 2 in Plates 8c and 8d), but anomalies are not always centered in the correct location (e.g., in Plate 8b the high of box 3), nor are the peak amplitudes (±0.2 km/s) always fully restored (e.g., Plate 8a the high in box 3 and the low in box 4).

The crust-mantle transition beneath the Aleutians is not a simple step-like discontinuity in the velocity field that would give rise to a specular P_mP reflection and a clear P_n diving wave. However, this is a convenient simplification for modeling of the crust/mantle transition; first-arrival inversion on its own will always result in the smoothest-possible velocity field, whereas a velocity discontinuity, once introduced into the model, will not be removed by subsequent inversion steps as long as it does not contradict the data. A velocity discontinuity also ensures that crustal (P_g and S_g) and mantle (P_n and S_n) refractions are separated; in a model without

Plate 3. Receiver line (Figure 1) cross section through (a) P wave and (b) S wave velocity models. Shaded area is constrained by rays within 12 km. Floating, unmarked solid lines mark modeled wide-angle reflectors in the crust and mantle where they are constrained by nearby reflection points. Moho and top of subducting slab (thick solid lines) are constrained where they intersect the shaded area. Arrows indicate intersections with other cross sections. The receiver locations that are connected by this profile are shown as black triangles. Velocity-depth function 4 (which is close to the profile) and the intersections with shot lines are marked by vertical lines. (c) Contours of V_p/V_s ratio in constrained area; contour interval is 0.02.

Moho discontinuity, mantle velocities tend to bleed into the least constrained parts of the lower crust giving rise to unrealistically high velocities there. Giving the P_mP reflection priority in the definition of the Moho allows refraction velocities below 7.6 km/s (the conventional definition of the refraction Moho) to appear below the Moho (Plate 4a at the location of velocity function 3). This suggests a reflective mafic layer at the base of the crust or a transition zone consisting of a mixture of mafic and ultramafic rocks.

The absence of a clear P_n phase can be seen, for example on receiver 4 (Figure 2a) recording shots from the west on line A2; the first arrival disappears at an offset of about 120 km, but P_mP is traceable to far greater offsets. Thus it often appears as if a reflected event is the first arrival. Furthermore, strong reflections arrive between P_mP and P_sP (one of these is modeled as $P_{mr}P$), indicating a heterogeneous arc mantle wedge. Because of the clear P_sP reflection, information about the velocity of the mantle wedge can be gained both from P_n, which constrains the uppermost part just below the Moho, and from P_sP, which provides a bulk velocity for the entire ray path above the subducting slab. Velocity inversion of the P_n and P_sP arrivals results in a mantle model that has the velocity increasing slowly from 7.4 to 7.9–8.2 km/s. An average velocity for the mantle wedge would be about 7.7 km/s (but note the high P_n velocity of 8.2 km/s at the Moho in Plate 4a at 300 km).

6. Results of Compressional Wave Traveltime Analysis

Velocities and crustal thickness vary only slightly along strike (Plates 3a and 4a). Most of these variations can probably be explained by the differences in ray coverage, but the decrease in velocity east of receiver 8 on Unalaska island in Plate 3a is probably a real feature as the ray coverage in this region is more uniform than farther west. Throughout the region, the most reflective zone between 10 and 20 km depth coincides generally with high velocities (6.8–7.4 km/s), whereas the crust below shows both high (up to 7.4 km/s) and low (6.6 km/s) velocities on a horizontal scale of about 100 km (smaller heterogeneities cannot be resolved as shown in Plate 8). Overall, the fore-arc, as sampled by the reflector line (Plate 4a) has higher velocities than the receiver line, which roughly follows the volcanic line (Plate 3a).

Across the arc, however, we observe a pattern that seems to be consistent along the studied segment; the middle and lower crust of the fore-arc is significantly faster (up to 7.4 km/s at 15 km depth) than the volcanic arc itself (as low as 6.7 km/s just above the Moho), whereas the back-arc as far as we see it in this study has an intermediate velocity under a thick sedimentary cover (Plates 5a and 6a). Small high-velocity bodies are found in the upper fore-arc on both the two eastern cross sections (Plates 5a and 6a). Section X618 (Plate 6a) shows decreasing velocities in the lower crust, starting at 17 km depth in the fore-arc and 25 km depth in the back-arc. In contrast, the westernmost cross section X462 shows a monotonous increase of velocity with depth (fore-arc only).

The crustal reflections not only separate zones with different seismic velocities and therefore composition but also most likely structures of different tectonic origin. In the best-resolved area around cross section X618 (Plate 6), the upper and lower reflectors enclose the highest crustal velocities. The thickness of this mid-crustal zone is 5–7 km. With a velocity of 7.1–7.4 km/s, it could represent preexisting Aleutia (Kula) oceanic crust (cumulate gabbros of oceanic layer 3) intruded by ongoing arc-magmatism in accordance with the conceptual model for the Aleutian Arc of *Kay and Kay* [1985, 1988]. This implies that the rest of the lower and upper crust represents the newly created arc crust. By accounting for most of the highest velocities as due to old oceanic crust, the net arc contribution becomes considerably more felsic or continent-like, but still overall mafic (see section on arc composition below). The high-velocity bodies are most pronounced to the north and the south of the volcanic line (receiver location), separated by a less than 30-km-wide zone of depressed velocities under the volcanos (e.g., Plate 6). This spatial coincidence of lower velocities with the receiver line is not an artifact of our inversion methodology; we tested inversions using starting models of both low and high velocity. Furthermore, the lower-crustal reflection P_5P can be seen to end abruptly in a high-amplitude diffraction (or reflection from an essentially vertical plane) on receiver 15 (Figures 2c and 3d; Plate 6 at Y = 80 km) as it approaches the volcanic line from the south. Whether the lower velocities in the volcanic zone are primarily due to locally higher temperatures or differences in bulk composition, our observations are consistent with the idea that active magmatic intrusion into the crust is confined to the volcanic line, feeding the volcanic centers vertically above. Smaller high-velocity bodies in the fore-arc shallow crust (e.g., Plate 4a at 320 and 415 km; Plate 6a at 45 km) may be arc-magmatic intrusions from an earlier magmatic episode when the volcanic zone was either wider or located more southerly in the present-day fore-arc. Some northward migration of the volcanic zone is also indicated by the northward younging of surface volcanics in the eastern Aleutians: Tertiary in the Krenitzin Islands and on the southside of Unalaska and Quaternary around the active volcanic centers on Akun, Akutan and the northside of Unalaska [*Beikman*, 1980].

Across-arc changes in mantle velocity cannot be resolved, whereas the along-arc variation between section X618 (7.6 km/s; Plate 6a) and sections X462 (Plate 7a) and X678 (7.8 km/s; Plate 5a) may well be real. Elevated temperatures in the mantle wedge under X618 are the most likely explanation. Akutan volcano (location

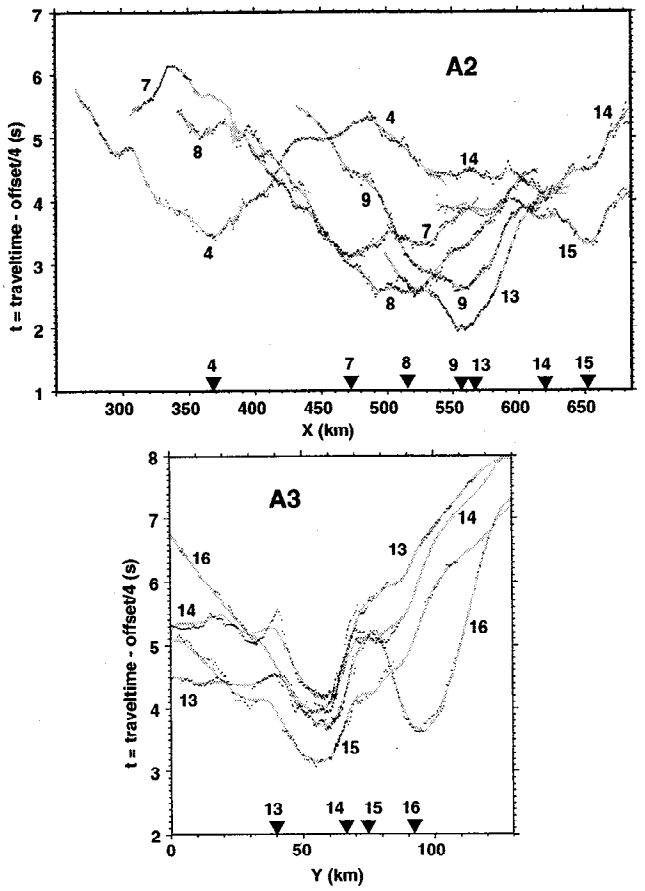

Figure 7. Picked (dots) and modeled (solid lines) traveltimes of S wave first arrivals reduced at 4.0 km/s. Only every tenth pick is plotted, and error bars have been omitted for clarity. Abscissa is model X coordinate for line A2 and model Y coordinate for line A3. Triangles mark receiver coordinates.

of receiver 14, 10 km west of X618) happens to be the most active volcano in the study area in historic time [*Fournelle et al.*, 1994].

There are several wide-angle mantle reflectors and the most prominent is modeled as shown in the cross sections. It is unclear what gives rise to the presumably high reflection coefficient of this well-defined (i.e., sharp) reflector since it is not connected with an obvious change in velocity. Ultramafic cumulates related to the arc magmatism would have the same seismic velocities as the underlying tectonized mantle; they are therefore indistinguishable from the latter unless they are reflective. One possibility is that $P_{mr}P$ indicates such a transition from petrologic crust to petrologic mantle (cumulate ultramafic rocks to tectonized ultramafic rocks) below the seismic Moho, but near-vertical seismic reflection images might be a better way to address this issue. More speculatively, $P_{mr}P$ could indicate a hydration (serpentinization) front, where the reflector is close to and conformable with the slab (Plates 4a and 7a), or a magma-generation front where the reflector is closer to the Moho (Plates 3a and 6a).

7. Shear Wave Arrivals

Stations 4, 7, 8, 9, 13, 14, 15, and 16 recorded good shear wave arrivals in lines A2 and A3 (Figure 7 shows a compilation of picked and modeled refracted arrivals), mainly S_g (Figures 2b and 3e), some S_n, and a few usable reflected arrivals ($S_{mr}S$, S_mS and S_5S, the lowermost intracrustal reflector which is usually stronger or as strong as the following Moho reflection). S_sS can usually not be seen because it arrives at the receivers at approximately the same time as the P wave of the following shot. We used the P wave velocity model as a starting model for shear-wave inversion by applying a uniform V_p/V_s ratio of 1.8 chosen because this ratio predicts fairly well the S arrival overall (*Miller and Christensen* [1994] found a V_p/V_s ratio of 1.77 for the Kohistan arc crust). At some offsets, the S arrival is substantially earlier than predicted, fitting a V_p/V_s ratio of about 1.74. The different V_p/V_s ratios likely reflect compositional differences in the arc crust. In typical crustal rocks, a low V_p/V_s ratio means a high quartz content or ultramafic composition (low plagioclase content) [*Christensen*, 1996], which is significant since the generally high P wave velocities point to a mafic bulk composition and petrological models for the lower crust require a high plagioclase content (30.4% normative anorthite and 23.7% normative albite) [*Taylor and McLennan*, 1995]; an An56 plagioclase has a V_p/V_s ratio of 1.853 from the Voigt-Reuss-Hill average [*Christensen*, 1996, and references therein]. V_p/V_s ratios in the Aleutians (Plates 3c and 4c) do not increase continuously from the surface to the Moho as a simple compositional progression from granite to gabbro would require. Instead, they reach a maximum in the midcrust (generally between 10 and 15 km depth) and decrease again in the lower crust. The V_p/V_s ratio below the Moho is not well constrained due to the sparse S_n data.

8. Velocity-Depth Functions

The first-order information that can be extracted from the traveltime tomography, and the results in which we have the highest confidence, are one-dimensional average velocity-depth curves for the entire study area or for single tectonic provinces. We obtain such curves in areas with good vertical ray coverage (Figure 8) by averaging columns of 20 by 20 grid-cells (24 by 24 km) both for P and S wave velocities.

Except for the shallow part of the back-arc function 5, crustal P wave velocities are high, mainly between 6.5 and 7 km/s, whereas sub-Moho velocities are unusually low (7.5–7.8 km/s). S wave velocities generally follow the same trend except for the S wave low-velocity zone at around 12 km depth for functions 2–4. Function 1 is from the island fore-arc, the other functions from the transition zone near the continental margin. Functions 2 and 3 (fore-arc) have a pronounced maximum at 15 km depth, function 4 (volcanic line) shows

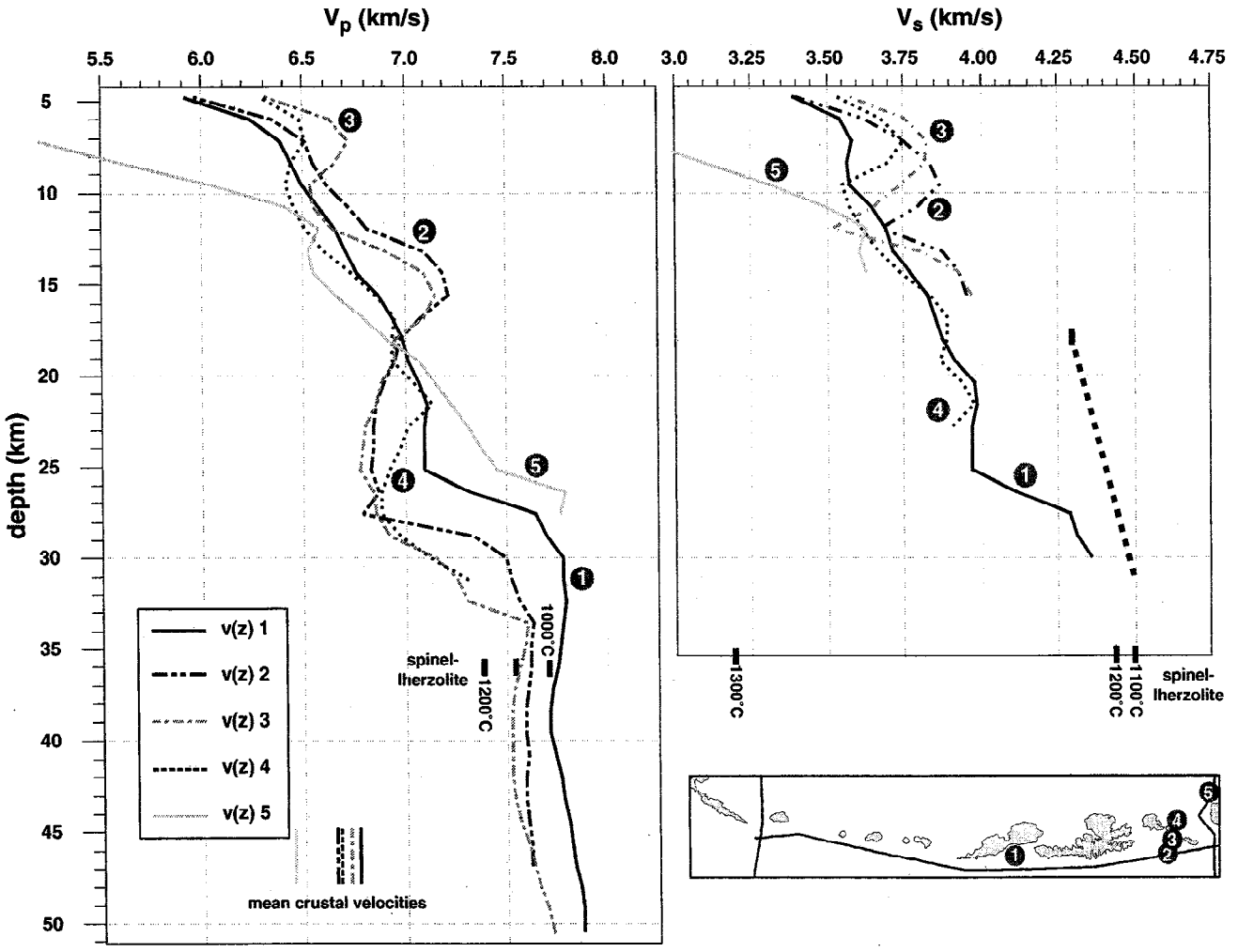

Figure 8. Velocity-depth functions extracted from the three-dimensional velocity models by averaging horizontally columns of 20 by 20 grid-cells. The lower end of each curve marks the depth of the deepest ray hitting each column. Velocities above 5 km are usually poorly constrained and not shown here. Mean crustal velocity (surface-to-Moho average) for each function is shown as a vertical bar. For locations of the functions see inset map or Figure 1. Tick marks at 36 km on the V_p diagram mark measurements on spinel lherzolite by *Murase and Kushiro* [1979] at (with decreasing velocity) 1000 °C, 1100 °C, and 1200 °C. The analogous V_s measurements [*Murase and Fukuyama,* 1980] are shown on the V_s diagram for 1100 °C, 1200 °C, and 1300 °C. The dashed line interpolates the 1100 °C values between measurements at 0.5 and 1 GPa.

increasing velocities similar to function 1 down to 22 km depth and decreasing velocities for most of the lower crust. The back-arc function 5 shows the most rapid increase of velocity with depth from the low surface velocities of the sedimentary back-arc basin to the highest lower-crustal velocities.

Average crustal P wave velocities (from the surface to the Moho) are 6.78 km/s for velocity function 1, 6.66 km/s for function 2, 6.73 km/s for function 3, 6.68 km/s for function 4, and 6.46 km/s for function 5.

The relationship between mineralogical composition and seismic velocity is far from unique apart from a general trend of velocity increasing with mafic content. For a given rock type, the seismic velocity depends mainly on temperature, pressure, and physical state. The pressure and temperature dependence of seismic velocities in solid rocks is well known from laboratory measurements (one of the most recent and most comprehensive compilations is *Christensen and Mooney* [1995]). These relations break down when the rocks start to melt. In spite of the great uncertainties that are therefore involved when one tries to associate seismic velocities with rock types, we will make the attempt in the following sections in order to arrive at a useful petrological interpretation of our seismic model. We restrict a priori the range of models that would satisfy the velocity constraints alone by making the following assumptions: (1) there is no partial melt in the arc crust (this assumption is certainly wrong for the upper mantle) and (2) the temperature profile of the arc is known well enough

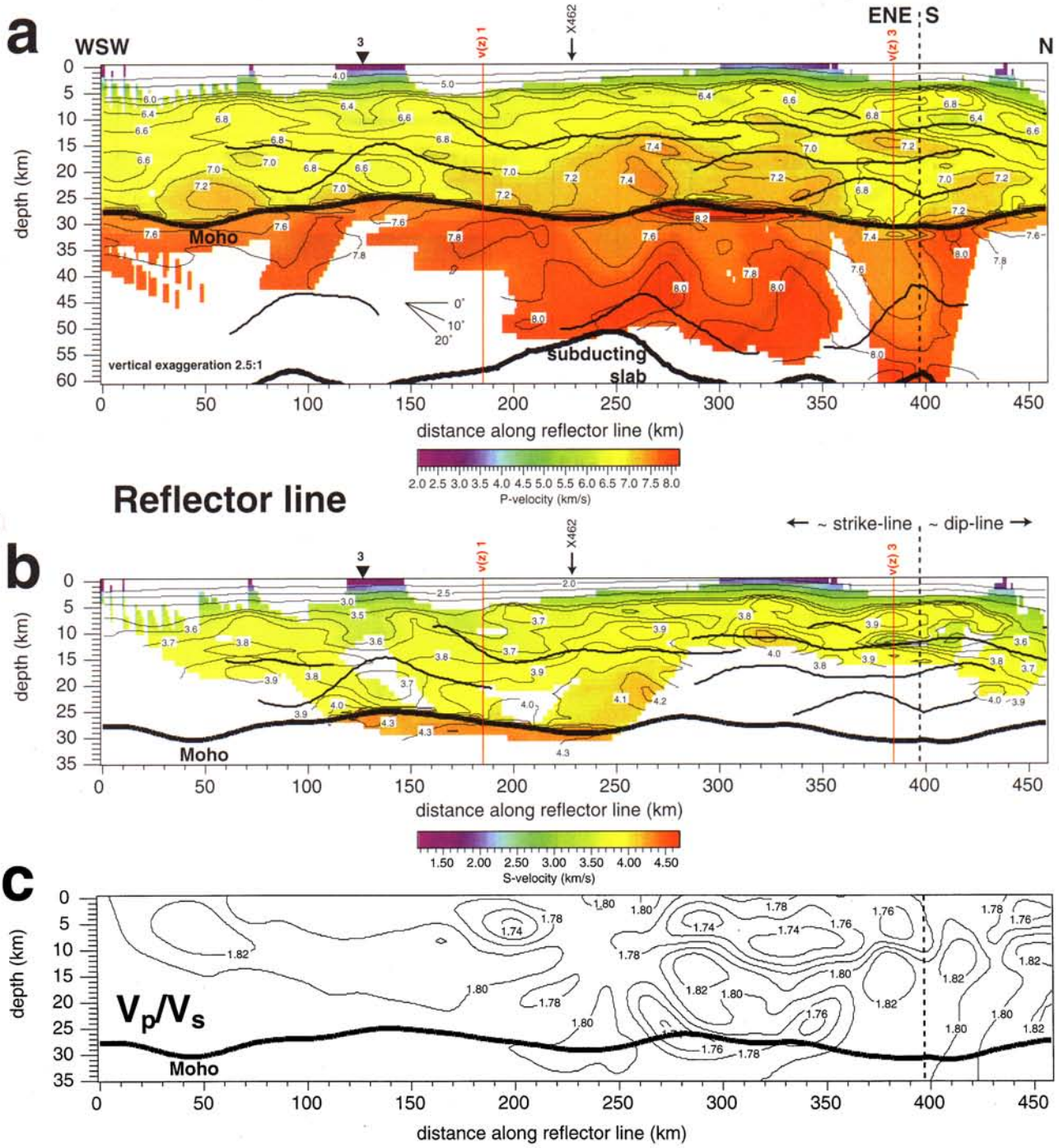

Plate 4. See caption to Plate 3; cross section is now along the reflector line (Figure 1). The sharp bend in the profile from a strike to a near-dip line is marked by a vertical dashed line.

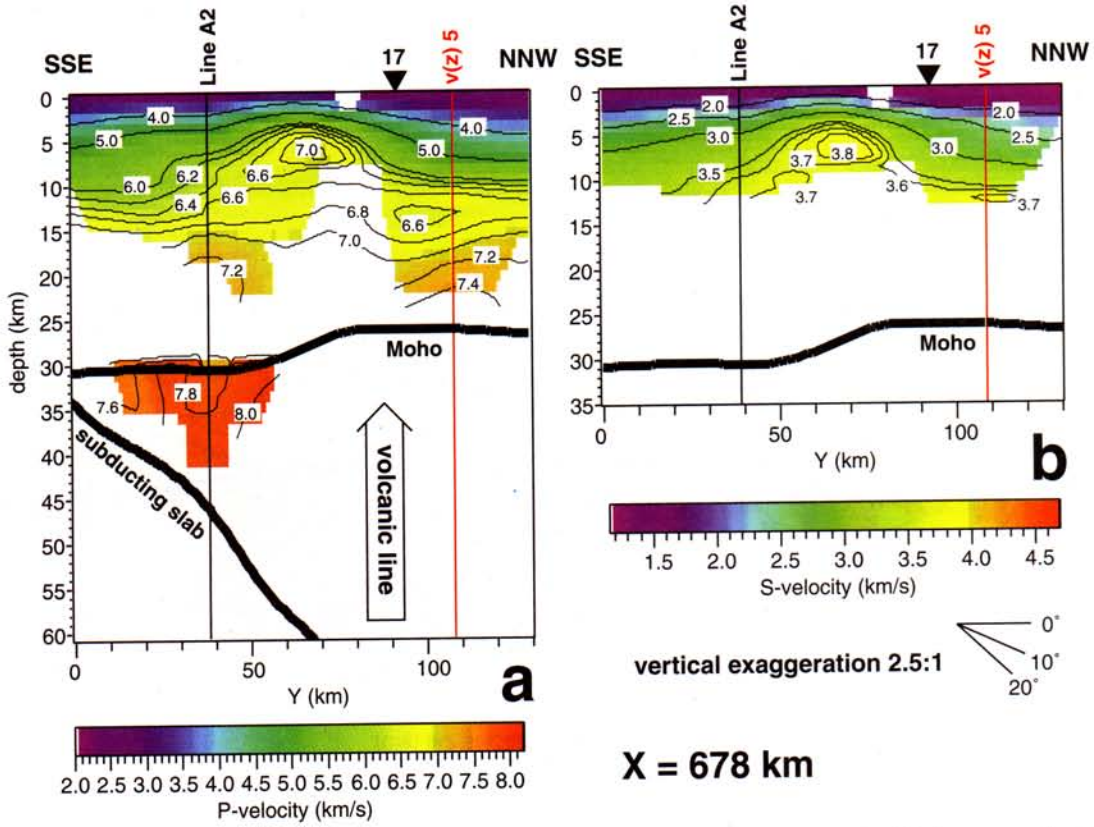

Plate 5. Cross section at model X coordinate 678 through (a) P wave and (b) S wave velocity models.

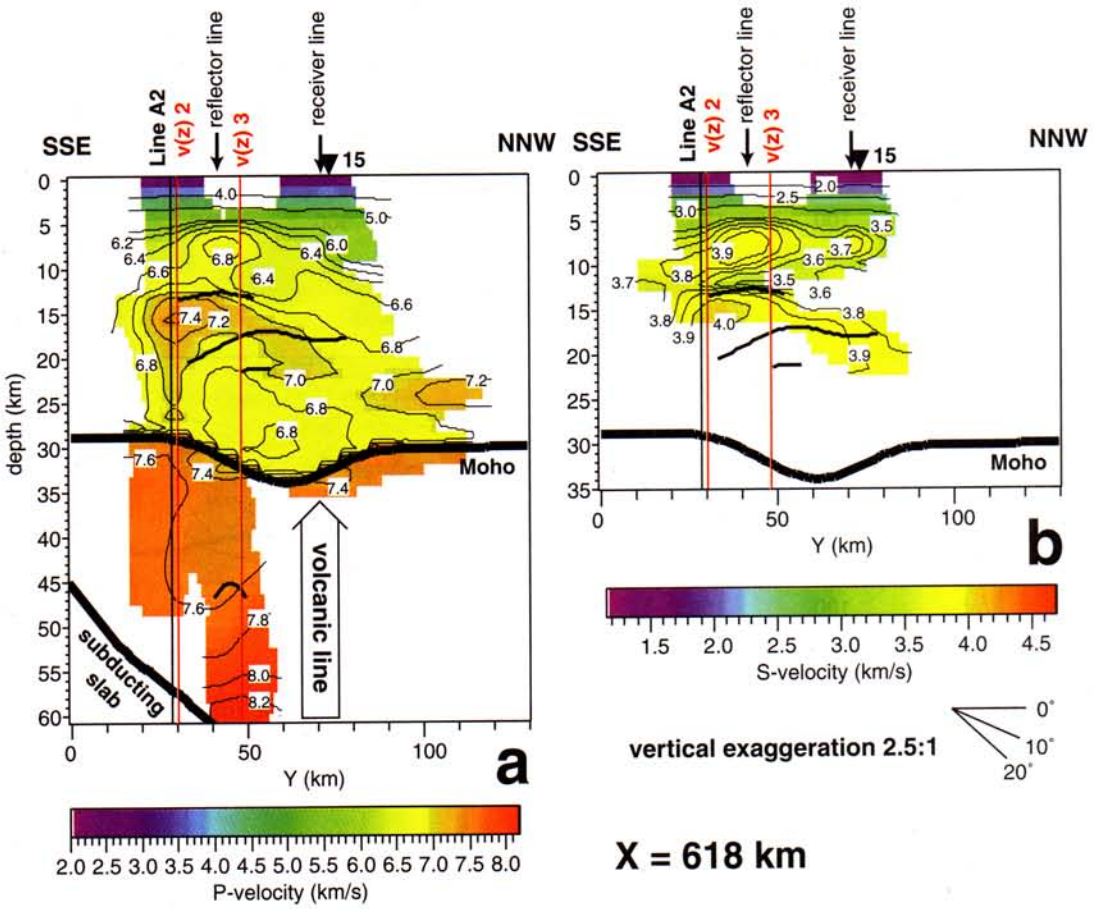

Plate 6. Cross section at model X coordinate 618 through (a) P wave and (b) S wave velocity models.

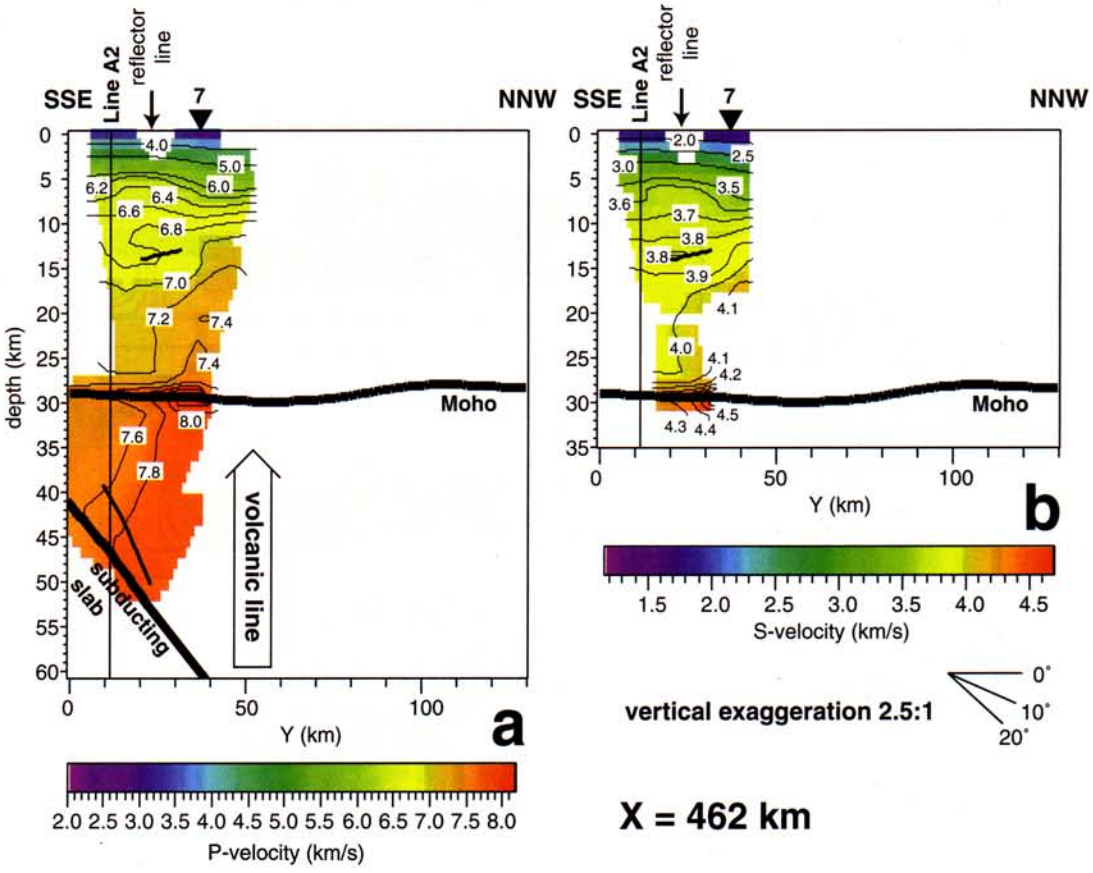

Plate 7. Cross section at model X coordinate 462 through (a) P wave and (b) S wave velocity models.

for our purpose. The following section is intended to justify the second assumption.

9. Thermal Regime of the Aleutian Arc

We know of only two heat flow measurements made in the Aleutian Arc: 54 mW/m^2 on Amchitka (450 km west of our study area, 50 km south of the volcanic line) [*Sass and Munroe,* 1970]; 69±16 mW/m^2 in the western Aleutian Arc [*Smirnov and Sugrobov,* 1982]. Measurements behind the arc in the Aleutian Basin yield a wide range of heat flow values, 42 to 195 mW/m^2, without any obvious geographic pattern [*Langseth et al.,* 1980].

Petrological studies give widely varying results for the thermal regime of arcs. Stability studies on pargasite found in Adagdak ultramafic xenoliths led *DeBari et al.* [1987] to conclude that 1050 °C is a rough upper limit for the temperature at the crust-mantle boundary. *DeBari and Coleman* [1989] found arc-Moho temperatures of 825 °C to 900 °C in equilibration studies on the Tonsina ultramafic-mafic assemblage (in the Peninsular terrane of southern Alaska, interpreted to have crystallized at the base of a mature oceanic island arc). The much higher temperatures necessary to produce basalt magmas from the mantle wedge need only be reached well below and north of the region of interest here (70–80 km depth beneath the volcanic line [*Kushiro,* 1987]).

Kushiro [1987] constructs a geotherm for Ichinomegata, a tuff cone at the coast of the Sea of Japan in the NE Honshu back-arc, which intersects the Basin and Range geotherm of *Blackwell* [1971] at a depth of 35 km, but stays well above it at shallower depths (Figure 9). Since the regional surface heat flow in the Sea of Japan is 80–100 mW/m^2 [*Smirnov and Sugrobov,* 1982], considerably higher than in the Aleutian Arc, we consider this geotherm an extreme upper bound.

Ponko and Peacock [1995] modeled the southern Alaska subduction zone for different initial geotherms and amounts of shear heating (Figure 9). Their warm end-member arc model (45 mW/m^2) seems to be the most appropriate for the Aleutian arc; it gives a Moho temperature considerably less than 800 °C, below the estimates of *DeBari and Coleman* [1989], and is similar to the eastern United States (15 °C/km) heat flow province of *Blackwell* [1971]. The *Ponko and Peacock* [1995] fore-arc model falls between the eastern United States and Sierra Nevada heat flow provinces of *Blackwell* [1971] and provides a lower bound for our study.

In order to model crustal composition from seismic

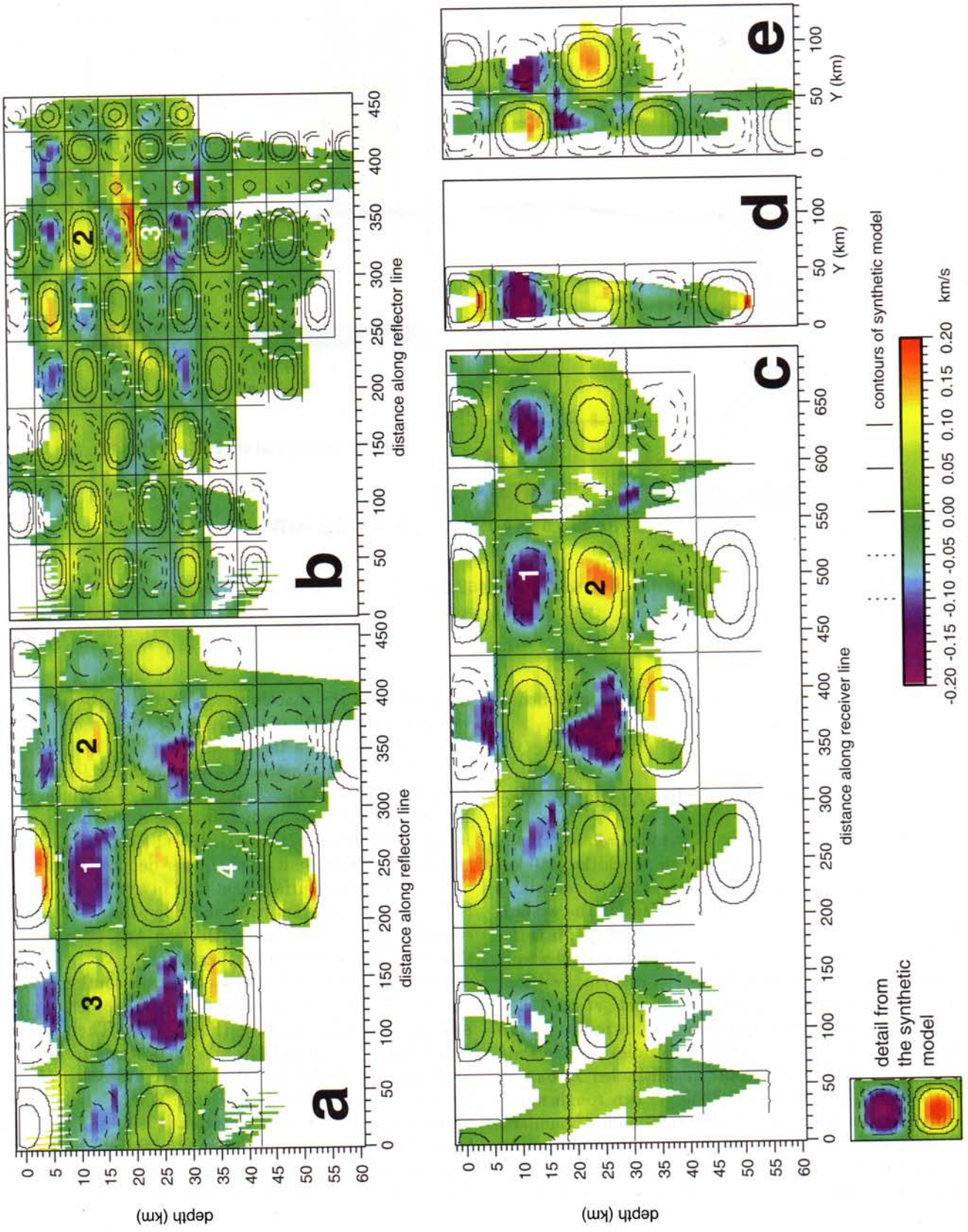
a
b
c
d
e
depth (km)
distance along reflector line
distance along receiver line
Y (km)
contours of synthetic model
km/s
-0.20 -0.15 -0.10 -0.05 0.00 0.05 0.10 0.15 0.20
detail from the synthetic model

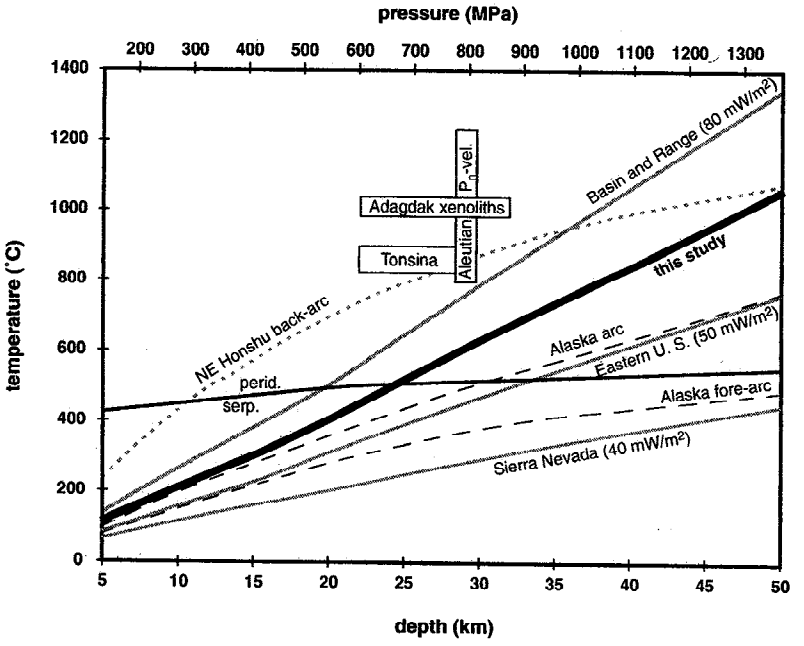

Figure 9. Geotherms discussed in the text. Sierra Nevada, Eastern United States, and Basin and Range geotherms (surface heat-flow in parentheses) are from *Blackwell* [1971]. The NE Honshu curve is from *Kushiro* [1987] and represents a back-arc setting. Alaska geotherms are from the warm end-member model of *Ponko and Peacock* [1995] (surface heat flow 48 mW/m^2). Serpentine stability curve (serp./perid.) from *Scarfe and Wyllie* [1967]. Moho temperature estimate (upper limit) from Adagdak xenoliths from *DeBari et al.* [1987]; estimate from Tonsina exposures from *DeBari and Coleman* [1989]. Moho temperature estimate from P_n-velocities is based on the temperature dependence of the P wave velocity in spinel lherzolite (Figure 8).

velocity, we have selected a single geotherm, 20 K/km, an average between the Basin and Range and Eastern United States geotherms of *Blackwell* [1971]. Despite the large uncertainties in lower-crustal temperatures, the consequent uncertainty in estimating composition from velocities is small. The temperature difference between the implausibly cold, Sierra Nevada geotherm and the implausibly hot, Basin and Range geotherm at a depth of 50 km is 900 °C; with a temperature coefficient typical for mafic rocks of −0.55 m/s/K, this gives a velocity range of ±0.25 km/s. Realistic temperature-induced differences at the arc and fore-arc Moho are less than ±0.12 km/s. The average standard deviation within each petrologic rock type of the laboratory measurements by *Christensen and Mooney* [1995] is 0.2 km/s. Taking also into account the about ±0.2 km/s uncertainties in our refraction velocity estimates, an error bar of ±0.3 km/s (±0.2 km/s to shear wave velocities in rough proportion with the lower velocities) will be applied uniformly to the rock velocities in the fol-

Plate 8. Checkerboard test of model resolution. A sinusoidal velocity perturbation of ±0.2 km/s (detail shown below the cross sections) is superimposed on a smoothed version of the final P wave velocity model. The reconstruction started with the unperturbed final velocity model, and inverted the traveltimes calculated from the synthetic model as observations. Displayed are the difference between the starting model and the synthetic (i.e., correct) model (contour lines) in comparison with the difference between the starting model and the inversion result (i.e., our best estimate of the synthetic model given the distribution of available data; colors). "Success" would be alternating blue and red bulls eyes as in the detail from the synthetic model, below left. Contour lines are 0.0 (rectangular grid of nodal planes), 0.05, and 0.1 km/s (positive solid, negative dashed) deviation of the synthetic model from the starting model. The synthetic model in Plates 8a, 8c, 8d, and 8e has a wavelength of 240 km in X, 120 km in Y, and 24 km vertically, in Plate 8b 120 km in X, 60 km in Y, and 12 km vertically. (a), (b) cross section coincident with reflector line section in Plate 4; Numbers on the plots refer to the main text. (c) cross section coincident with receiver line section in Plate 3; (d) cross section coincident with section at X = 462 km in Plate 5; (e) cross section coincident with section at X = 618 km in Plate 6.

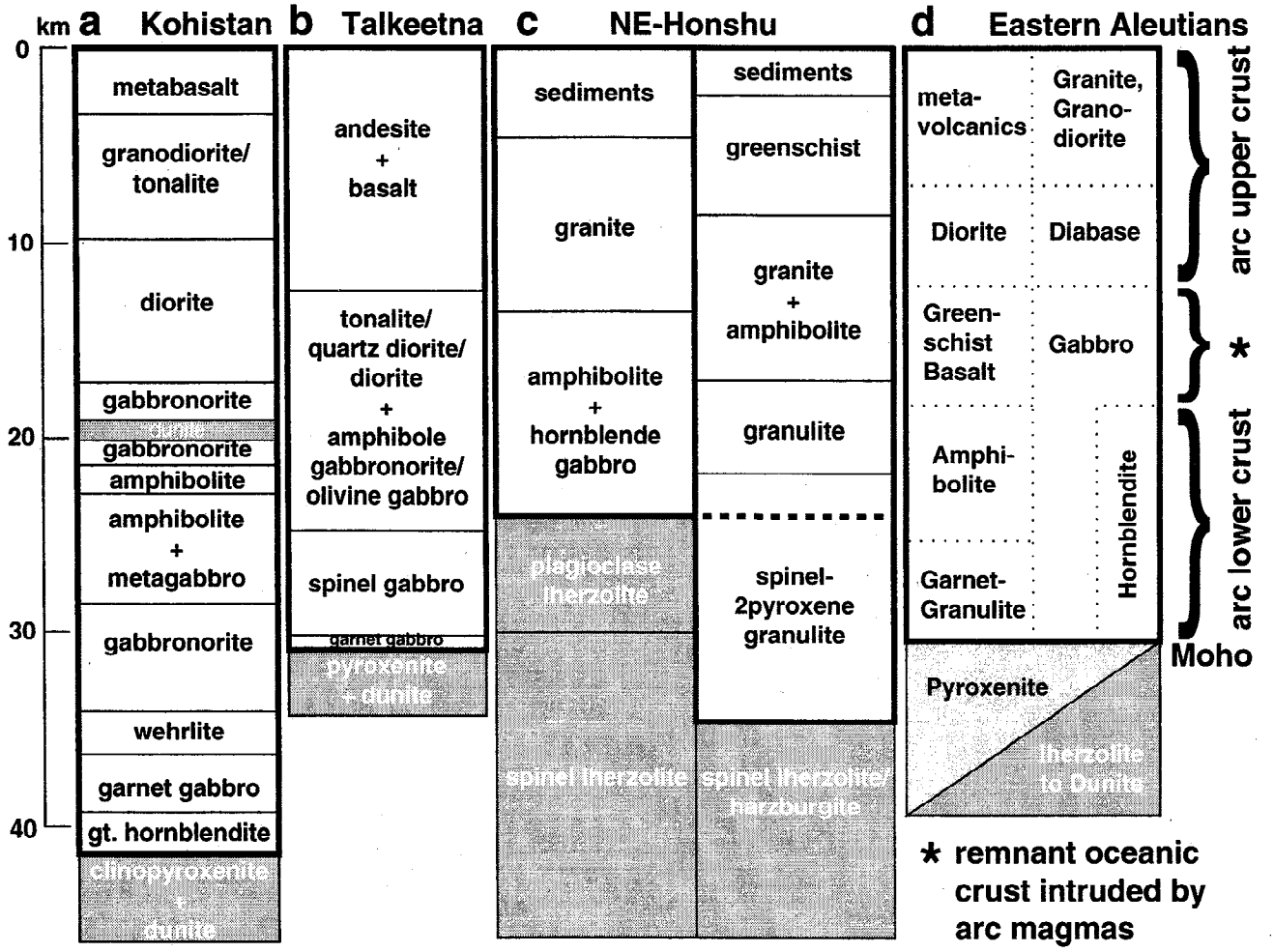

Figure 10. Schematic petrologic columns for four island arcs: (a) Kohistan in Pakistan [*Miller and Christensen,* 1994], (b) Talkeetna in southern Alaska [*DeBari and Sleep,* 1991], (c) northeastern Honshu in the Japan arc [left *Takahashi,* 1978; right *Kushiro,* 1987], and (d) the eastern Aleutian Arc (this study) based on one-dimensional velocity functions (Plate 8) and rock type matches (Figures 11 and 12). Capitalized rock names in Figure 10d correspond to the categories of *Christensen and Mooney* [1995]. The heavy frame encloses the part of the section that corresponds to the seismic crust with the Moho at the base. The Talkeetna arc is now structurally thinned and so the lithologic column has been stretched (by a factor of 3) to match the crustal thickness of the Aleutian column. The dashed line in the *Kushiro* [1987] column indicates the location of the Moho earlier in the development of the arc: the spinel granulite layer grows at the expense of the uppermost mantle.

lowing analysis. A variable error measure that depends on temperature, depth, and composition may be more rigorous, but the use of a single error parameter greatly simplifies the display of the comparison without leading to qualitatively different results for the geological interpretation.

10. Temperature of the Mantle Wedge

It is not a priori certain that the seismic Moho coincides with the petrologic crust-mantle boundary, in other words, the sub-Moho layer could represent eclogite- or granulite-facies mafic crustal rocks, or crustal peridotitic cumulates, rather than mantle peridotite [*Jarchow and Thompson,* 1989; *Griffin and O'Reilly,* 1987; *Mengel and Kern,* 1992; *Herzberg et al.,* 1983]. However, under the assumption that peridotite is the velocity-determining rock type at sub-Moho depths, we can use our velocities to estimate the arc-mantle temperature. *Murase and Kushiro* [1979] and *Murase and Fukuyama* [1980] measured V_p and V_s of a spinel lherzolite to 1 GPa and 1300 °C compared in Figure 8 with five representative velocity-depth functions from the eastern Aleutians (see below). The observed P wave velocities at 36 km depth match a lherzolite of 950°–1100 °C; incorporating ±0.3 km/s variations allows a range of c. 800°–1250 °C. Our only available sub-Moho S velocity observation (Plate 4b and Figure 8) suggests temperatures >1100 °C (higher temperatures cannot be sensibly interpolated between 0.5 and 1 GPa because of

the sharp drop of shear wave velocities with the start of partial melting at lower pressures), although incorporating a ±0.2 km/s variation allows a temperature down to about 1000 °C. Since this S wave velocity function comes from the fore-arc, these temperature estimates seem too high, whereas the estimates from V_p alone fall within the range of petrologic estimates. The disagreement between temperature estimates from P and S waves could indicate that the upper mantle is partially molten (and S wave velocities are more sensitive to the presence of small amounts of liquid) or the chosen lherzolite is a poor representative for the probed mantle region (though the database both of laboratory and field measurements is too inadequate for a meaningful assessment).

Alternatively, and articularly in the fore-arc, the Moho temperature could be much lower and serpentinization could account for low sub-Moho velocities (see stability curve in Figure 9) and possibly also for the observed mantle reflectivity (see above).

11. Arc Composition From One-Dimensional Velocity Functions

Some of the best characterized descriptions of exposed island arcs are those of the Kohistan terrane [*Miller and Christensen,* 1994], the Talkeetna island arc, Alaska [*DeBari and Sleep,* 1991], and the Japan arc [*Takahashi,* 1978, and *Kushiro,* 1987] (Figure 10). All these columns have in common a felsic-to-intermediate

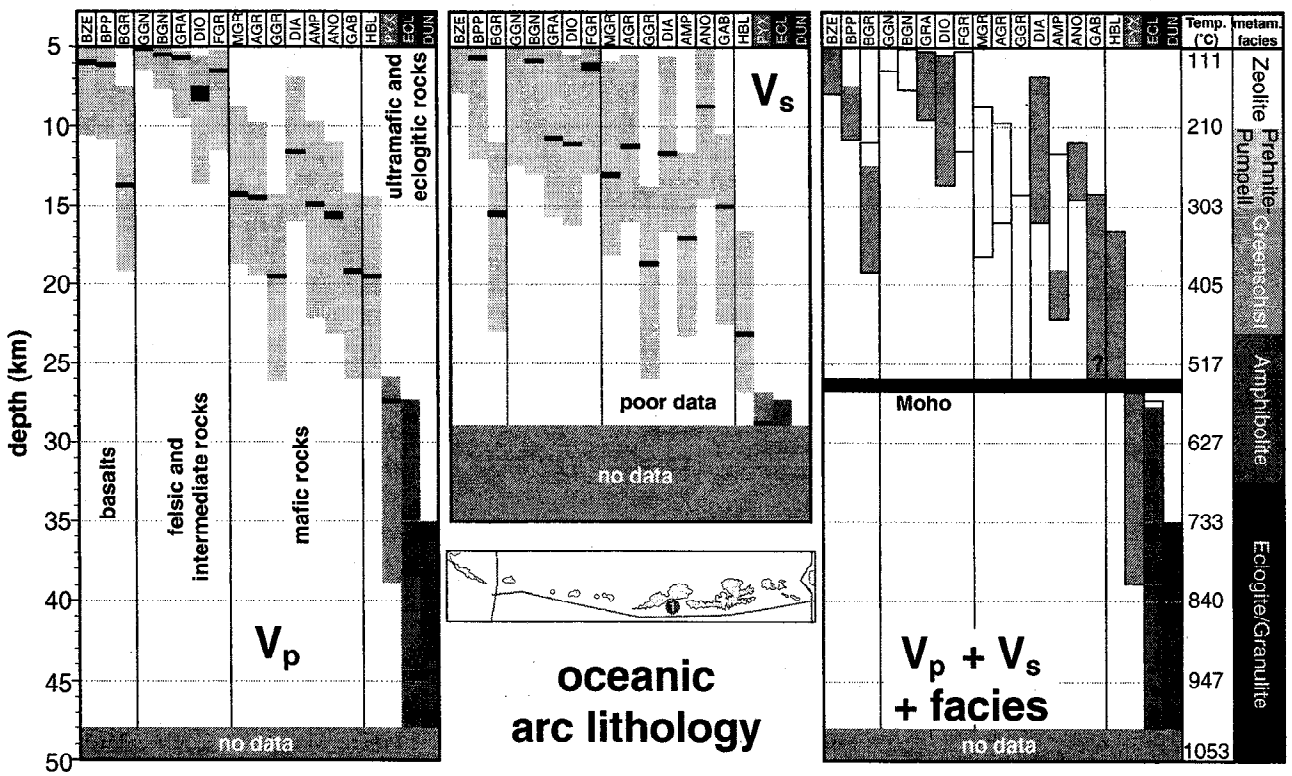

Figure 11. Depth range in which different rock types fit velocity-depth function 1 (Figure 8; location in Figure 1). Rock types and abbreviations at the head of the diagram are from *Christensen and Mooney* [1995] and *Christensen* [1996]: BZE Zeolite Facies Basalt, BPP Prehnite-Pumpellyite Facies Basalt, BGR Greenschist Facies Basalt, GGN Granite Gneiss, BGN Biotite (Tonalitic) Gneiss, GRA Granite and Granodiorite, DIO Diorite, FGR Felsic Granulite, MGR Mafic Granulite (garnet-free), AGR Anorthositic Granulite, GGR Garnet-bearing Mafic Granulite, DIA Diabase, AMP Amphibolite, ANO Anorthosite, GAB Gabbro/Norite/Troctolite, HBL Hornblendite, PYX Pyroxenite, ECL Mafic Eclogite, DUN Dunite. Black bars mark the depth where the laboratory mean for a rock category matches the value of our measured velocity function at that depth. Gray bars indicate the depth range in which the laboratory mean does not deviate more than (left) ±0.3 km/s for V_p and (middle) ±0.2 km/s for V_s from the velocity function. The depth range below which S wave raypaths are sparse is labeled "poor data"; S wave constraints from this depth range were not used to construct the right panel. The right panel shows the depth range in which each rock type satisfies both the P and S wave velocity functions (where available) as outlined boxes and as gray boxes for metamorphic rocks that also satisfy the appropriate metamorphic facies condition (see main text). Darker shades of gray are mantle rocks. The question mark indicates that the range of Gabbro would be more restricted if the "poor" S wave data were used.

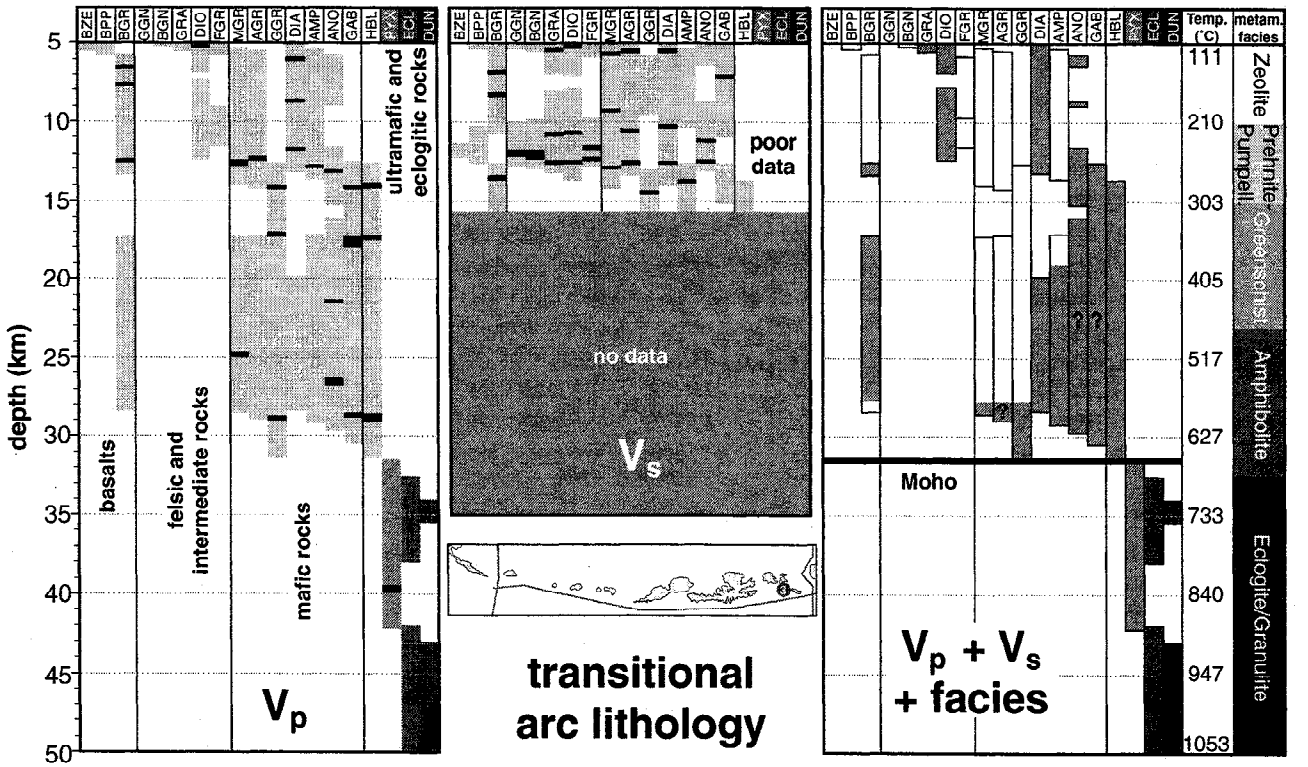

Figure 12. Depth range in which different rock types fit velocity-depth function 3 (Plate 8; location in Figure 1; for caption and abbreviations see Figure 11). Question marks indicate ranges that are based on V_p only because of the lack of S wave coverage but that would have been eliminated if the V_s trend (middle) was extrapolated downward.

upper crust over a mafic lower crust that accounts for at least half of the crustal column.

In order to fit a petrological model to our velocity model, we use the compilations of P and S wave velocities for crustal rocks of *Christensen and Mooney* [1995] and *Christensen* [1996]. We exclude sedimentary and metasedimentary rocks that are not expected to be widespread in an arc setting, volcanic rocks because we do not consider the upper 5 km of the crust, and serpentinite, which does not fit the observed crustal velocities under the inferred temperature condition. That leaves 19 common igneous and metamorphic rock types categorized by *Christensen and Mooney* [1995], capitalized in the following discussion to distinguish them from the generic use of the same names. The S wave velocity compilation of *Christensen* [1996] does not contain measurements at different temperatures; we therefore use the measurements of V_p/V_s ratios by *Christensen* [1996], which are practically independent of temperature, to convert the appropriate P wave velocities from *Christensen and Mooney* [1995]. We show rock-type diagrams only for velocity functions 1 and 3 (Figures 11 and 12); additional diagrams are given by *Fliedner* [1997].

Figures 11 and 12 show the large number of acceptable alternative compositions at each depth if only P wave or only S wave velocities are available. However, there is no significant overlap in the depth ranges of mafic rock types and of ultramafics (+ Mafic Eclogite), so a seismic Moho can always be clearly defined.

Where we have both P wave and good S wave coverage, we can determine the depth ranges that satisfy both velocity measurements simultaneously. In addition we can narrow the ranges of metamorphic rocks by restricting them to the pT conditions of their metamorphic facies (right-hand panel in Figures 11 and 12); since the Aleutian Arc is still intact, we can rule out significant vertical movements that would bring high-grade rocks to shallower levels. This condition, of course, can only be applied loosely because the stability fields for the different facies are not tightly constrained and overlap. We therefore retain all metamorphic rocks that fit either the appropriate facies at a particular depth or the adjacent half of the next higher or lower facies. Furthermore, we do not differentiate between the granulite and eclogite facies because our geotherm falls in between the two fields (facies fields taken from *Fyfe et al.* [1978]).

The upper crust (5–12 km) can be described by a relatively wide range of plutonic rock types from felsic to mafic with the oceanic-island fore-arc (Figure 11) at the felsic and the ocean-continent transitional fore-arc (Figure 12) at the mafic end of the range: Granite to Basalt (at low metamorphic grade). The midcrust (12–18 km), which has the highest crustal velocities and is in greenschist facies is best described by Greenschist Facies Basalt, Gabbro, Anorthosite, or Hornblendite. In the

lower crust (18 km to Moho), since the S wave coverage is poor, our inferences are based on P wave velocities: Hornblendite, Amphibolite, Anorthosite, Gabbro, and, close to the base of the crust Anorthositic or Garnet-bearing Mafic Granulites.

Weak additional constraints come from the (poorly constrained) relatively low V_p/V_s ratios (Plates 3 and 4), which if correct rule out plagioclase-rich rocks, and the non-occurrence of garnet in any of the lower crustal or upper mantle xenoliths from Adak in the central Aleutians [*DeBari et al.*, 1987], which if relevant rules out garnet-granulite in our lower crust. The crust just south of the volcanic line (Figures 11 and 12) can most simply (though not uniquely) be described by just two rock types: a Diabase upper crust and a Hornblendite (or Gabbro, although this fits less well with the S wave velocities) lower crust (Figure 10d).

Directly below the Moho, Pyroxenite and Mafic Eclogite are the possible rock types, whereas Dunite becomes a possibility below about 35 km depth. The Mafic Eclogite (a crustal layer below the Moho) is only compatible with the lower temperature estimates for the crust-mantle boundary, and is not compatible with the garnet-free xenoliths of Adak.

12. Comparison With Exposed Arc Terranes

The results of the preceding section are summarized schematically in Figure 10d for comparison with other arc systems (Figures 10a, 10b, and 10c). The uppermost unit in our Aleutian upper crust most closely resembles Kohistan. Our Aleutian midcrust (Greenschist Basalt or Gabbro) is somewhat comparable with both Kohistan and Talkeetna which are dominated by gabbro. An equivalent to the Kohistan midcrustal dunite layer has not been found in any of the other columns, but the trend to have the highest velocities in the midcrust is also seen in the Aleutian Arc. The velocities, V_p/V_s ratio, and thickness of our Aleutian midcrustal layer are more similar to oceanic crust than any other part of the arc. We therefore identify this layer with the layer of remnant oceanic crust in the Aleutian Arc model of *Kay and Kay* [1985] while recognizing that arc magmatism must have modified the original crust and destroyed its integrity. At the location of the present-day volcanic line, this higher-velocity layer is indeed practically absent (Plate 6a). Our Aleutian lower crust is similar to the Honshu arc (amphibolite and granulite) and, to a lesser degree to the Kohistan lower crust which is still dominated by gabbro. Our Aleutian uppermost mantle grading from Pyroxenite to peridotite is directly comparable with Talkeetna or Kohistan.

13. Conclusions

Our wide-angle experiment shows that the eastern Aleutian island arc is comparable to exposed sections of accreted terranes (e.g., Talkeetna in southern Alaska or Kohistan in northern Pakistan) that are assumed to be of island-arc origin, thereby giving additional support to

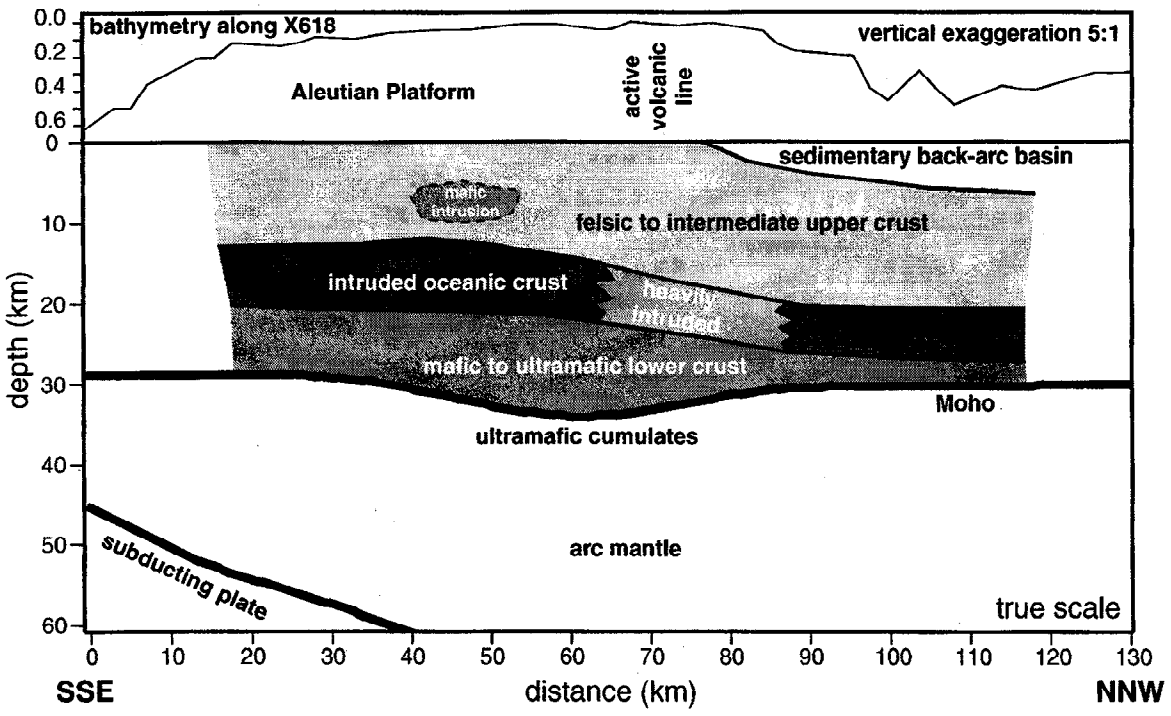

Figure 13. Cartoon cross section through the eastern Aleutian Arc based on our three-dimensional velocity models (particularly section X618, Plate 6). The volcanic front marks the line of active volcanos (X618 runs between Akutan and Akun). Top shows bathymetry along line X618.

that interpretation. Figure 13 (based on section X618, Plate 6) summarizes the results in cartoon fashion.

The Aleutian crust, with the Moho at about 30 km, is almost continental in thickness and consists of about 20% preexisting oceanic crust, 40% felsic to intermediate arc upper crust (the upper unresolved half of that probably mainly andesitic volcanics), and 40% mafic to possibly ultramafic arc lower crust. It is much thicker than the 20-km-thick Izu-Ogasawara oceanic island arc, which has been studied with similar methods [*Suyehiro et al.*, 1996]. The difference is due to a thicker mafic lower crust in the Aleutians. The Izu-Ogasawara arc also lacks the high-velocity zone in the middle crust that we interpret as modified oceanic crust in the Aleutian arc; to the contrary, the Izu-Ogasawara middle crust (confined behind the volcanic front) shows velocities around 6 km/s, which is indicative of a granitic composition [*Suyehiro et al.*, 1996].

The reflective character of the uppermost mantle may indicate layers of ultramafic cumulates or of serpentinization. *Conrad and Kay* [1984] calculated that primitive mantle-derived basalt fractionates into 79% high-alumina basalt that is added to the crust and 21% ultramafic cumulates below the Moho. With about 24 km of added material in the Aleutian crust (Figure 10d), this calculation predicts a 5-km-thick cumulate layer, too little for our modeled mantle reflector to represent simply the base of arc-related ultramafic cumulates.

Active intrusive magmatism, if this is indeed represented by depressed seismic velocities, is restricted to a about 30 km wide zone at the volcanic front (Plate 6). It is not clear whether the arc is hot enough to be in granulite facies in the lower crust; the low upper mantle velocities could support these higher temperatures but could equally well be due to a composition dominated by pyroxene instead of olivine. Along-strike variations in the seismic structure are small in the area covered by this study; the Aleutian Islands preserve a uniform island-arc character right up to the ocean/continent transition as marked by the Bering shelf edge.

Christensen and Mooney [1995] concluded that continental crust has an average V_p of 6.45±0.23 km/s, which is significantly less than we find for the Aleutian arc and fore-arc (6.7 km/s). It appears therefore that accretion of complete island arcs cannot alone be responsible for crustal growth. It is, however, possible that repeated cycles of subduction and arc magmatism as occurred in the continental Aleutian Arc lower the average velocity (increase the proportion of felsic to intermediate crustal material) to more continent-like values. True continental arcs like the Andes [*Zandt et al.*, 1994] or the Sierra Nevada of California [*Fliedner et al.*, 1996] have much lower average velocities (about 6.0 km/s) and are therefore more felsic.

Acknowledgments. This experiment has been supported by NSF (Geophysics Program) grant EAR-92-04998. The instruments were provided by IRIS/PASSCAL. Steve Holbrook and Dan Lizarralde kindly provided us with the OBS data. Sue McGeary, John Diebold, Nathan Bangs, and the scientific party of *R/V Ewing* cruise 94-09 conducted the marine seismic-reflection survey that provided the source for our recordings. We thank Aleutian Airlines of Dutch Harbor, AK, for safe air transportation and the native corporations for permission to work on their land. We thank Sue DeBari, Nik Christensen, and Roberta Rudnick for their comments and advice on petrological questions.

References

Abers, G. A., Three-Dimensional inversion of regional P and S arrival times in the East Aleutians and sources of subduction zone gravity highs, *J. Geophys. Res.*, *99*(B3), 4395–4412, 1994.

Beikman, H. M., Geologic map of Alaska, scale 1:2,500,000, *U.S. Geol. Surv. Spec. Map*, 1980.

Blackwell, D. D., The thermal structure of the continental crust, in *The Structure and Physical Properties of the Earth's Crust*, Geophys. Monogr. Ser., vol. 14, edited by J. G. Heacock, pp. 169–184, AGU, Washington, D. C., 1971.

Boyd, T. M., and K. C. Creager, The geometry of Aleutian subduction: Three-dimensional seismic imaging, *J. Geophys. Res.*, *96*(B2), 2267–2291, 1991.

Brocher, T. M., G. S. Fuis, M. A. Fisher, G. Plafker, M. J. Moses, J. J. Taber, and N. I. Christensen, Mapping the megathrust beneath the northern Gulf of Alaska using wide-angle seismic data, *J. Geophys. Res.*, *99*(B6), 11663–11685, 1994.

Carder, D. S., D. Tocher, C. Bufe, S. W. Stewart, J. Eisler, and E. Berg, Seismic wave arrivals from Longshot, *Geol. Soc. Am. Bull.*, *57*(4), 573–590, 1967.

Christensen, N. I., Poisson's ratio and crustal seismology, *J. Geophys. Res.*, *101*(B2), 3139–3156, 1996.

Christensen, N. I., and W. D. Mooney, Seismic velocity structure and composition of the continental crust: A global view, *J. Geophys. Res.*, *100*(B6), 9761–9788, 1995.

Conrad, W. K., and R. W. Kay, Ultramafic and mafic inclusions from Adak Island: Crystallization history, and implications for the nature of primary magmas and crustal evolution in the Aleutian Arc, *J. Petrol.*, *25*(1), 88–125, 1984.

Cooper, A. K., M. S. Marlow, and D. W. Scholl, Mesozoic magnetic lineations in the Bering Sea Marginal Basin, *J. Geophys. Res.*, *81*(11), 1916–1934, 1976.

Creager, K. C., and T. M. Boyd, The geometry of Aleutian subduction: Three-dimensional kinematic flow model, *J. Geophys. Res.*, *96*(B2), 2293–2307, 1991.

DeBari, S. M., and R. G. Coleman, Examination of the deep levels of an island arc: Evidence from the Tonsina ultramafic-mafic assemblage, Tonsina, Alaska, *J. Geophys. Res.*, *94*(B4), 4373–4391, 1989.

DeBari, S. M., and N. H. Sleep, High-Mg, low-Al bulk composition of the Talkeetna island arc, Alaska: Implications for primary magmas and the nature of arc crust, *Geol. Soc. Am. Bull.*, *103*(1), 37–47, 1991.

DeBari, S., S. M. Kay, and R. W. Kay, Ultramafic xenoliths from Adagdak Volcano, Adak, Aleutian Islands, Alaska: Deformed igneous cumulates from the Moho of an island arc, *Journal of Geology*, *95*, 329–341, 1987.

Engdahl, E. R., and D. Gubbins, Simultaneous travel time inversion of earthquake location and subduction zone structure in the central Aleutian Islands, *J. Geophys. Res.*, *92*(B13), 13855–13862, 1987.

Espinosa, A. F., and K. S. Rukstales, Geometry of the Benioff zone and mode of subduction beneath southwestern Alaska and the Aleutian Islands, *U. S. Geol. Surv., Misc. Invest. Ser. Map, I-1945*, 1988.

Fisher, M. A., R. von Huene, G. L. Smith, and T. R. Bruns,

Possible seismic reflections from the downgoing Pacific Plate, 275 kilometers arcward from the eastern Aleutian Trench, *J. Geophys. Res., 88*(B7), 5835–5849, 1983.

Fliedner, M. M., Making of continental crust by arc magmatism: Wide-angle seismic and gravity studies in the southern Sierra Nevada of California and the eastern Aleutian Arc, Ph.D. thesis, Stanford Univ., Stanford, Calif., 1997.

Fliedner, M. M., S. Ruppert, and SSCD Working Group, Three-dimensional crustal structure of the southern Sierra Nevada from seismic fan profiles and gravity modeling, *Geology, 24*(4), 367–370, 1996.

Fournelle, J. H., B. D. Marsh, and J. D. Myers, Age, character, and significance of Aleutian arc volcanism, in *The Geology of Alaska,* edited by G. Plafker, and H. C. Berg, pp. 723–757, Geol. of N. Am. vol. G-1, Geol. Soc. of Am., Boulder, Colo., 1994.

Fyfe, W. S., N. J. Price, and A. B. Thompson, *Fluids in the Earth's Crust,* Elsevier, New York, 1978.

Griffin, W. L., and S. Y. O'Reilly, Is the continental Moho the crust-mantle boundary?, *Geology, 15*(3), 241–244, 1987.

Grow, J. A., Crustal and upper mantle structure of the central Aleutian Arc, *Geol. Soc. Am. Bull., 84*(7), 2169–2192, 1973.

Hamilton, W. B., Crustal evolution by arc magmatism, *Philos. Trans. R. Soc. London, 301,* 279–291, 1981.

Herzberg, C. T., W. S. Fyfe, and M. J. Carr, Density constraints on the formation of the continental Moho and crust, *Contrib. Mineral. Petrol., 84,* 1–5, 1983.

Holbrook, W. S., W. D. Mooney, and N. I. Christensen, The seismic velocity structure of the deep continental crust, in *Continental Lower Crust,* edited by D. M. Fountain, R. Arculus, and R. W. Kay, pp. 1–43, Elsevier, New York, 1992.

Holbrook, W. S., D. Lizarralde, S. McGeary, J. Diebold, N. Bangs, and S. L. Klemperer, Wide-angle ocean-bottom seismic data from the Aleutian Arc: Preliminary results of the 1994 Survey (abstract), *Eos Trans. AGU, 75*(44), 643, 1994.

Hole, J. A., Nonlinear high-resolution three-dimensional seismic travel time tomography, *J. Geophys. Res., 97*(B5), 6553–6562, 1992.

Hole, J. A., and B. C. Zelt, 3-D finite-difference reflection traveltimes, *J. Geophys. Res., 121*(2), 427–434, 1995.

Jarchow, C. M., and G. A. Thompson, The nature of the Mohorovicic discontinuity, *Ann. Rev. Earth Plant. Sci., 17,* 475–506, 1989.

Kay, R. W., and S. M. Kay, Crustal recycling and the Aleutian arc, *Geochim. Cosmochim. Acta, 52,* 1351–1359, 1988.

Kay, R. W., and S. M. Kay, Delamination and delamination magmatism, *Tectonophysics, 219*(1–3), 177–189, 1993.

Kay, S. M., and R. W. Kay, Role of crystal cumulates and the oceanic crust in the formation of the lower crust of the Aleutian arc, *Geology, 13*(7), 461–464, 1985.

Kushiro, I., A petrological model of the mantle wedge and lower crust in the Japanese island arcs, in *Magmatic Processes: Physiochemical Principles,* edited by B. O. Mysen, pp. 165–181, Geochem. Soc., University Park, Penns., 1987.

Langseth, M. G., M. A. Hobart, and K. Horai, Heat flow in the Bering Sea, *J. Geophys. Res., 85*(B7), 3740–3750, 1980.

Lizarralde, D., W. S. Holbrook, N. Bangs, S. McGeary, S. Klemperer, and M. Fliedner, Crustal Structure of a Proto-Continental Volcanic Arc: Eastern Aleutians (abstract), *Eos Trans. AGU, 77*(46), F659, 1996.

Marlow, M. S., and A. K. Cooper, Wandering terranes in southern Alaska: The Aleutia microplate and implications for the Bering Sea, *J. Geophys. Res., 88*(B4), 3439–3446, 1983.

McGeary, S., N. L. Bangs, and Aleutian Working Group, Seismic reflection images of the deep structure of the Aleutian Arc and subducting slab (abstract), *Eos Trans. AGU, 76*(46), 593, 1995.

Mengel, K., and H. Kern, Evolution of the petrological and seismic Moho—implications for the continental crust-mantle boundary, *Terra Nova, 4*(1), 109–116, 1992.

Miller, D. J., and N. I. Christensen, Seismic signature and geochemistry of an island arc: A multidisciplinary study of the Kohistan accreted terrane, northern Pakistan, *J. Geophys. Res., 99*(B6), 11623–11642, 1994.

Motyka, R. J., and C. J. Nye, *A Geological, Geochemical, and Geophysical Survey of the Geothermal Resources at Hot Springs Bay Valley, Akutan Island, Alaska,* 115 pp., State of Alaska, Dep. of Natural Resour., Div. of Geol. and Geophys. Surv., Juneau, 1988.

Murase, T., and H. Fukuyama, Shear wave velocity in partially molten peridotite at high pressures, *Carnegie Inst. Wash. Yearb., 79,* 307–311, 1980.

Murase, T., and I. Kushiro, Compressional wave velocity in partially molten peridotite at high pressures, *Carnegie Inst. Wash. Yearb., 78,* 559–562, 1979.

Nelson, K. D., Deep seismic profiling and continental evolution, in *Continental Lithosphere: Deep Seismic Reflections,* edited by R. Meissner, L. Brown, H.-J. Duerbaum, W. Franke, K. Fuchs, and F. Seifert, pp. 377–382, AGU, Washington, D. C., 1991.

Ponko, S. C., and S. M. Peacock, Thermal modeling of the southern Alaska subduction zone: Insight into the petrology of the subducting slab and overlying mantle wedge, *J. Geophys. Res., 100*(B11), 22117–22128, 1995.

Reymer, A., and G. Schubert, Phanerozoic addition rates to the continental crust and crustal growth, *Tectonics, 3*(1), 63–77, 1984.

Sass, J. H., and R. J. Munroe, Heat flow from deep boreholes on two island arcs, *J. Geophys. Res., 75*(23), 4387–4395, 1970.

Scarfe, C. M., and P. J. Wyllie, Serpentine dehydration curves and their bearing on serpentinite deformation in orogenesis, *Nature, 215,* 945–946, 1967.

Scholl, D. W., T. L. Vallier, and A. J. Stevenson, Geologic evolution and petroleum potential of the Aleutian Ridge, in *Geology and Resource Potential of the Continental Margin of Western North America and Adjacent Ocean Basins; Beaufort Sea to Baja California,* edited by D. W. Scholl, A. Grantz, and J. G. Vedder, pp. 123–156, Circum-Pacific Council for Energy and Mineral Resources, Houston, Tex., 1987.

Shor, G. G., Structure of the Bering Sea and the Aleutian ridge, *Marine Geology, 1,* 213–219, 1964.

Smirnov, Y. B., and V. M. Sugrobov, Terrestrial heat flow in the northwestern Pacific, *Tectonophysics, 83,* 109–122, 1982.

Smithson, S. B., R. A. Johnson, and Y. K. Wong, Mean crustal velocity: A critical parameter for interpreting crustal structure and crustal growth, *Earth Planet. Sci. Lett., 53*(3), 323–332, 1981.

Suyehiro, K., N. Takahashi, Y. Ariie, Y. Yokoi, R. Hino, M. Shinohara, T. Kanazawa, N. Hirata, H. Tokuyama, A. Taira, Continental crust, crustal underplating, and low-Q upper mantle beneath an oceanic island arc, *Science, 272,* 390–392, 1996.

Takahashi, E., Petrological model of the crust and upper mantle of the Japanese Island Arcs, *Bull. Volcanol., 41*(4), 529–547, 1978.

Taylor, S. R., and S. M. McLennan, The geochemical evolu-

tion of the continental crust, *Rev. Geophys., 33*(2), 241–265, 1995.

Vallier, T. L., D. W. Scholl, M. A. Fisher, T. R. Bruns, F. H. Wilson, R. von Huene, and A. J. Stevenson, Geologic framework of the Aleutian arc, Alaska, in *The Geology of Alaska*, edited by G. Plafker, and H. C. Berg, pp. 367–388, Geol. of N. Am. vol. G-1, Geol. Soc. of Am., Boulder, Colo., 1994.

Vidale, J. E., Finite-difference calculation of traveltimes in three dimensions, *Geophysics, 55*, 521–526, 1990.

Zandt, G., A. A. Velasco, and S. L. Beck, Composition and thickness of the southern Altiplano crust, Bolivia, *Geology, 22*(11), 1003–1006, 1994.

M. M. Fliedner, Bullard Laboratories, University of Cambridge, Madingley Road, Cambridge CB3 0EZ, United Kingdom. (email: moritz@esc.cam.ac.uk)

S. L. Klemperer, Department of Geophysics, Stanford University, Stanford, CA 94305-2215. (e-mail: klemp@pangea.stanford.edu)

(Received August 14, 1997; revised March 26, 1998; accepted April 27, 1998.)